



Title	Automated multimode phase speed measurements for high-resolution regional-scale tomography: application to North America
Author(s)	Yoshizawa, K.; Ekström, Göran
Citation	Geophysical Journal International, 183(3), 1538-1558 <a href="https://doi.org/10.1111/j.1365-246X.2010.04814.x">https://doi.org/10.1111/j.1365-246X.2010.04814.x</a>
Issue Date	2010
Doc URL	<a href="http://hdl.handle.net/2115/52165">http://hdl.handle.net/2115/52165</a>
Type	article
File Information	j.1365-246X.2010.04814.x.pdf



[Instructions for use](#)

# Automated multimode phase speed measurements for high-resolution regional-scale tomography: application to North America

K. Yoshizawa<sup>1,2</sup> and Göran Ekström<sup>1</sup>

<sup>1</sup>Lamont-Doherty Earth Observatory, Columbia University, Palisades, NY 10964, USA. E-mail: kazu.yoshizawa@mail.sci.hokudai.ac.jp

<sup>2</sup>Earth and Planetary Dynamics, Faculty of Science, Hokkaido University, Sapporo 060-0810, Japan

Accepted 2010 September 15. Received 2010 September 3; in original form 2009 July 20

## SUMMARY

A fully automated method for obtaining multimode phase speed measurements from a single seismogram has been developed and applied to a large data set of three-component long-period seismograms in North America, constructing high-resolution phase speed maps on a continental scale. The method of our phase speed estimation is based on a fully non-linear waveform inversion by Yoshizawa & Kennett working with a global search method (the Neighbourhood Algorithm). The entire process of waveform fitting and the evaluation of the estimated phase speed have been fully automated employing several empirical quantitative measures, assessing the quality of waveform fit and the relative contributions of each mode in a chosen time window. The measured phase speed data undergo automatic screening for quality control, comprising the threshold evaluation of their reliability and outlier detection and removal. This new automated method has been applied to a large data set recorded at North American stations, including the latest transportable stations of USArray. Using long-period three-component seismograms recorded during the past eight years, we have successfully retrieved large numbers of regional surface wave paths, including over 20 000 paths for the fundamental-mode Rayleigh waves over a wide range of frequencies, and over 10 000 paths for the higher mode Rayleigh as well as the fundamental-mode Love waves. The consistent results of the automated measurement procedure suggest that the method works well at regional distances, allowing us to perform a high-resolution mapping of multimode phase speeds in North America. The results of the automated waveform analysis also indicate some intrinsic limitations in the higher mode phase speed measurements from a single seismogram particularly in the short period range, mainly due to the overlapping of higher mode arrivals as well as coupling between mode branches. Despite such an innate difficulty in the higher mode dispersion measurements, the automated method allows us to construct reliable multimode phase speed maps. The current data set of ray paths is significantly biased towards the western half of North America, resulting in non-uniform horizontal resolution across the continent. This issue will be resolved by the future migration of the USArray stations to cover the central and eastern United States. The new automated method can be a useful tool for high-resolution mapping of regional 3-D shear wave structure including possible anisotropy.

**Key words:** Inverse theory; Surface waves and free oscillations; Seismic tomography; North America.

## 1 INTRODUCTION

Seismic surface waves provide us with fundamental knowledge about the Earth's upper mantle, and have been used to retrieve upper-mantle structure on global and regional scales. There are several ways to extract 3-D shear wave structure from surface waves. One of the common approaches is based on the direct measurements of path-average phase or group speeds of the fundamental-mode surface waves. Such an approach has been popular in global-scale modelling of the upper mantle with a large data set (e.g. Trampert

& Woodhouse 1995; Ekström *et al.* 1997; Ritzwoller *et al.* 2002; Nettles & Dziewonski 2008). The dispersion measurements of the fundamental mode are relatively straightforward, but they are, even at long periods, primarily sensitive to the structure above 300 km depth. The higher modes are more sensitive to the deep structure of the Earth (Fig. 1), and can provide information that is valuable for enhancing the vertical resolution of shear wave speed models from surface waves.

The higher mode information can be used in a framework of waveform fitting, which does not require the isolation of each mode

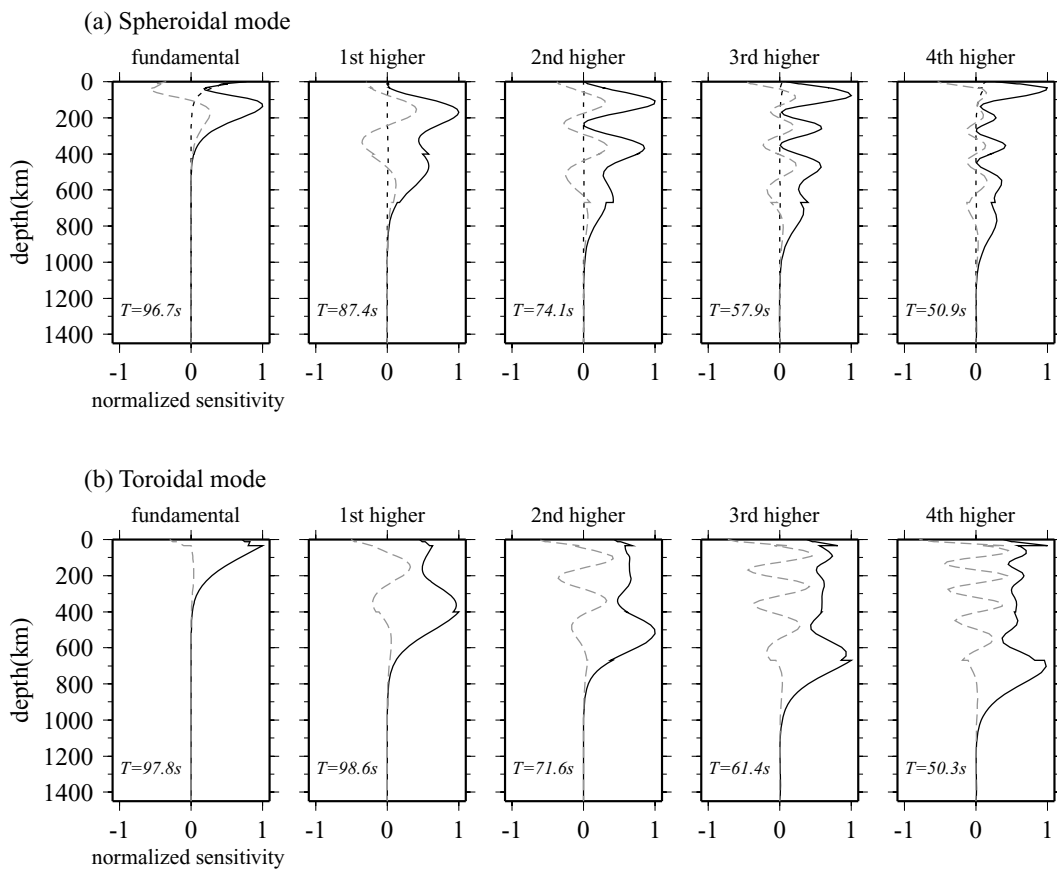


**Figure 1.** Vertical sensitivity kernels of (a) spheroidal and (b) toroidal modes calculated for PREM. The solid line is the sensitivity of phase speed to  $S$ -wave speed  $K_\beta$ , the dotted line to  $P$ -wave speed  $K_\alpha$  and the grey dashed line to density  $K_\rho$ . All the sensitivity kernels are normalized so that the maximum amplitude of  $K_\beta$  for each mode becomes unity.

in a seismogram. A partitioned waveform approach has been popular in regional-scale tomography, in which path-average 1-D models are constrained by waveform fitting with suitably filtered seismograms or cross-correlograms (e.g. Nolet 1990; Cara & L ev eque 1987). These 1-D models are then used to constrain the 3-D models. This kind of two-stage approach has been applied to many regions of the Earth for constructing regional 3-D shear wave speed models (e.g. van der Lee & Nolet 1997; Debayle & Kennett 2000a; Lebedev *et al.* 2005; van der Lee & Frederiksen 2005; Fishwick *et al.* 2008; Bedle & van der Lee 2009), and, in most cases, only Rayleigh waves are employed, while Love waves are rarely used with few exceptions (e.g. Debayle & Kennett 2000b). In such partitioned waveform methods, the 1-D models derived from waveform fitting are used as an average structure along a specific path (normally the great-circle path). Therefore, it is not simple to incorporate the frequency-dependent information such as the off-great-circle propagation in heterogeneous media and finite-frequency effects.

More rigorous ways of tomographic mapping, incorporating complex effects of wave propagation in a 3-D structure through the full waveform fitting, can also be used to constrain the large-scale upper-mantle structure (e.g. Li & Romanowicz 1996; Takeuchi 2007; Fichtner *et al.* 2008; Marone *et al.* 2007). Such approaches are theoretically more rigorous, but computationally demanding for high-resolution mapping with a very large data set.

To exploit the theoretical superiority of the finite-frequency approach, while taking account of the computational efficiency using a large data set, a multimode dispersion measurement would be

of great help for constraining a 3-D shear wave structure in the upper mantle. Such an approach has been proposed by Kennett & Yoshizawa (2002) and Yoshizawa & Kennett (2004) as a three-stage inversion, recasting the conventional method of two-stage regional surface wave tomography into three independent stages. In this approach, we can constrain the 3-D shear wave speed models in an efficient manner incorporating a variety of information such as the multimode information, off-great-circle propagation and finite-frequency effects of surface waves.

Information on multimode dispersion is essential for enhancing the vertical resolution of surface wave tomography models, but measuring higher mode dispersion from a single seismogram is a complicated issue. To achieve reliable multimode dispersion measurements, Stutzmann & Montagner (1993) used a group of seismograms recorded at a station from several seismic events at different depths in a small epicentral area. This method requires similar source–receiver pairs with seismic events at different source depths, which tends to limit the number of available paths.

One of the practical ways for measuring higher mode phase speeds was developed by van Heijst & Woodhouse (1997, 1999) employing a mode-branch stripping technique based on the fitting of mode-branch cross correlations. This technique is effective especially in the case of long paths for which higher mode branches do not overlap each other in a seismogram (van Heijst & Woodhouse 1999). However, this method cannot readily be applied to regional-scale studies for which the average length of the paths is shorter

than 50°, and individual contributions of higher modes cannot be discriminated in an observed seismogram.

An alternative way to estimate the multimode phase speeds from a single seismogram, regardless of the distance from the seismic source, has been proposed by Yoshizawa & Kennett (2002a) based on a fully non-linear waveform fitting method with the neighbourhood algorithm (hereafter referred to as NA) of Sambridge (1999a). In this method, we use the path-specific 1-D shear wave speed profile as model parameters for the waveform inversion, but we do not consider such path-specific 1-D models as direct representation of the average structure of the Earth along the path. Instead, we consider them as summaries of multimode dispersion for the source–receiver path, and use such 1-D models to estimate the multimode dispersion.

A similar method has recently been employed by Visser (2008) to estimate multimode dispersion curves for global-scale tomographic studies (Visser *et al.* 2007, 2008). The basic procedure of Visser is similar to that of Yoshizawa & Kennett (2002a), but they added a robust method of error estimation based on a Bayesian approach working with the extensive model parameter search using the second stage of NA (Sambridge 1999b). This process provides rigorous estimates for uncertainties in the phase speed measurements, though such resampling of model parameters with the NA tends to be computationally expensive.

In this study, we propose a fully automated method for making multimode phase speed measurements, extending the method originally developed by Yoshizawa & Kennett (2002a). We introduce some new quantitative parameters for evaluating the measured phase speeds, so that the method can be applied efficiently to the rapidly expanding data sets from dense seismic arrays. In such an automated analysis with a large data set, it is almost inevitable that some outliers are included in the measured phase speed data. We will also consider an automated detection and removal of such outliers to better constrain the phase speed maps.

The fully automated method of multimode phase speed measurements is then applied to a large number of seismograms recorded on the transportable network of the USArray, as well as at the permanent seismic stations in and around North America. The new method allows us to gather large numbers of regional paths of both Rayleigh and Love waves, which are subsequently used to construct phase speed models of North America with unprecedented resolution. The main objective of this paper is to summarize the new automated method for multimode dispersion measurements and its application to the large data set currently available in North America. Thus, obtaining a 3-D shear wave model using these phase speed maps is beyond the scope of this study, but will be considered in future work.

## 2 METHOD OF MULTIMODE PHASE SPEED MEASUREMENTS

In this study, we use an extended version of the method of multimode phase speed measurements developed by Yoshizawa & Kennett (2002a), which is based on fully non-linear waveform fitting working with a global search method. We employ the NA of Sambridge (1999a) which enables us to explore a model parameter space effectively to fit the observed and synthetic seismograms.

The details of original method, including the practical aspects of the non-linear model parameter search with the NA, are described by Yoshizawa & Kennett (2002a). In Section 2.1, we briefly summarize the basic principles of how we implement the non-linear waveform fitting and extract path-specific phase speed. In the subsequent sections, new aspects of the improved method of waveform

fitting, including empirical parameters for quantitative evaluation of the measured data are described.

### 2.1 Non-linear waveform fitting: synthetics and model parameters

A synthetic seismogram  $u(\Delta, \omega)$  in the frequency domain at epicentral distance  $\Delta$  and frequency  $\omega$  in heterogeneous media can be represented as follows, based on the WKBJ approximation (Woodhouse 1974; Tromp & Dahlen 1992; Dahlen & Tromp 1998):

$$u(\Delta, \omega) = \sum_{j=0}^N R_j(\omega) \exp \{i (k_j^0(\omega) + \delta k_j(\omega)) \Delta\} S_j(\omega), \quad (1)$$

where  $R_j$  is the receiver term of  $j$ -th mode, including geometrical spreading and attenuation, and  $S_j$  is the source excitation of  $j$ -th mode with an appropriate moment tensor at the event location. The exponential term represents the propagation along a path with a reference wavenumber  $k_j^0$  of the  $j$ -th mode in the reference model and the perturbation of the wavenumber  $\delta k_j$  caused by a lateral heterogeneity along the path.  $N$  is the number of mode branches used in the calculation of full synthetic seismograms. We use up to 25 modes for the calculation of synthetics in this study.

The wavenumber perturbation  $\delta k_j$  can be represented by a radial integration of structural perturbations of  $S$ -wave speed  $\delta\beta$ ,  $P$ -wave speed  $\delta\alpha$  and density  $\delta\rho$ , multiplied by the corresponding sensitivity kernels.

$$\begin{aligned} \delta k_j(\omega) &= \int_0^a \{K_\alpha^j(r, \omega) \delta\alpha(r) + K_\beta^j(r, \omega) \delta\beta(r) + K_\rho^j(r, \omega) \delta\rho(r)\} dr, \end{aligned} \quad (2)$$

where  $a$  is the Earth's radius,  $K_\alpha$ ,  $K_\beta$  and  $K_\rho$  represent the sensitivity kernels of surface-wave phase speed for  $P$ -wave speed,  $S$ -wave speed and density, respectively. Some examples of the vertical sensitivity kernels are shown in Fig. 1. Surface waves are sensitive mostly to  $S$ -wave speed perturbations, and the contributions from  $P$ -wave speed and density are relatively small. In many practical applications, only  $S$ -wave speed is considered as an independent parameter, and  $P$ -wave speed and density perturbations are generally ignored or scaled to the  $S$ -wave speed perturbation as explained in Section 3.2.

The shear wave speed perturbation  $\delta\beta(r)$  is represented by a set of B-spline functions  $\mathcal{B}(r)$  as a function of radius  $r$  (Fig. 2),  $\delta\beta(r) = \sum_{i=1}^M b_i \mathcal{B}_i(r)$ . The coefficients  $b_i$  are the model parameters that are searched by the NA to find models with smaller misfits or global minima. We sample 3050 1-D  $S$ -wave models with the NA, including 50 initial models that are randomly distributed in the model parameter space. The model parameter search using the NA is iterated 300 times, sampling 10 new models in each iteration based on the previous samples. The ensemble of over 3000 models derived from the NA normally provides satisfactory convergence of waveform fit between the synthetic and observed waveforms.

Although the NA does not require any linearization of the inverse problem to be solved, we use the linearized relation of phase perturbations with eq. (2). To reduce a computational cost for calculating normal modes, we employ a single reference starting model to compute the reference eigenfunctions. Model parameters are then searched using the NA, allowing up to about  $\pm 8$  per cent of shear wave speed perturbations from the reference model.

The reference model for waveform inversion is constructed from PREM (Preliminary Reference Earth Model; Dziewonski

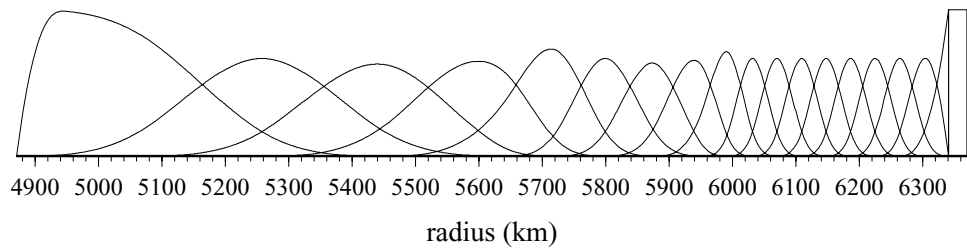


**Figure 2.** A set of B-spline functions for representing shear wave speed perturbations in the Earth's mantle. Node spacing is increasing with depth so that wave speed perturbations in the deeper part of the mantle vary smoothly.

& Anderson 1981) with a smoothed 220 km discontinuity. The crustal structure is corrected using a path-average crustal model derived from the *a priori* model 3SMAC (Nataf & Ricard 1996). If over 50 per cent of the path length traverses continental areas, the structure of the uppermost mantle above 220 km is replaced with that of PREM, which is a modified version of PREM, to better represent the uppermost mantle beneath the continental lithosphere.

It should be noted that the choice of the crust model does not have significant influence on the estimated phase speed in this study, because shear wave speed in the crust is also varied to better fit waveforms. Moreover, the purpose of our waveform fitting is to extract a better phase dispersion, and not to obtain a realistic 1-D wave speed profiles. The starting models used in the application of the non-linear waveform fitting are discussed in detail in Section 3.2.

## 2.2 Evaluation of waveform misfit

Waveform misfits of synthetic and observed seismograms are evaluated in several time windows using multiple bandpass filters to constrain the path-specific 1-D models, which are subsequently used for estimating multimode phase speeds.

Fig. 3 shows two examples of the waveform fit after inversion of Rayleigh waves at the J13A station of the USArray in Idaho, and Love waves at the nearby J12A station. In this study, all three components (vertical, radial and transverse) are inverted independently. We have used four time windows for Rayleigh waves, and three time windows for Love waves, which are defined by specific group speeds as summarized in Table 1. For windows including higher mode arrivals, which normally follow the *S*- or *SS*-wave arrivals depending on the epicentral distances, the start time of the window is determined with respect to the arrival time of the *S* or *SS* wave predicted from the AK135 model (Kennett *et al.* 1995), in a similar way to the window selection of Visser (2008).

In our non-linear waveform inversion, we use both the waveforms and the corresponding envelopes to evaluate waveform misfits. The simultaneous fitting of both waveform and envelope helps to reduce the likelihood of a possible phase cycle skip caused by large perturbations from the starting models during the non-linear model parameter search.

Misfit function  $\Phi_{ij}$  between synthetic and observed waveforms as well as envelopes for *i*-th time window with *j*-th bandpass filter is calculated using the similar definition given in the original work (see eq. (5) of Yoshizawa & Kennett 2002a), except that we normalize the misfit by the length of each time window  $T_w$ .  $\Phi_{ij}$  are then summed and averaged for all time windows and frequency bands to estimate the 'total waveform misfit  $\Phi$ ', which represents the average misfit of multiple time windows from a single seismogram.  $\Phi$  is used in the first step of quality control of our automated measurements.

Empirical selection thresholds for this parameter are discussed in Section 2.3.

Fig. 3 displays some examples of waveform fitting and Fig. 4 the 1-D shear wave speed model and the estimated phase speeds. As suggested by Yoshizawa & Kennett (2002a), the phase speeds estimated from non-linear waveform fitting are fairly robust, while the 1-D shear wave model itself tends to reflect a significant non-uniqueness. This effect is apparent in Fig. 4 in which all the 3050 models derived from the non-linear inversion are displayed with colours representing the misfit values. In this example, the best 500 *S*-wave models in yellow lines (Fig. 4a), tend to be scattered over the wide range of parameter space, while the corresponding dispersion curves (Fig. 4b), derived from the corresponding *S*-wave models, are concentrated around the best fit model displayed by the red lines. This suggests the robustness of the phase dispersion curves estimated from non-unique 1-D shear wave speed profiles.

## 2.3 Reliability of multimode phase speed measurements

An issue of measuring multimode phase speed from a single seismogram is that quantitative evaluation of errors and accuracy of the dispersion measurements is not very simple. Visser *et al.* (2007) employed the second stage of the NA (Sambridge 1999b) for a Bayesian statistical evaluation of the measurement errors, which is rigorous but is computationally demanding, since it requires extensive resampling of model parameters to estimate meaningful errors.

As a computationally efficient way to estimate the quality of the measurements, we use the reliability parameter (e.g. van Heijst & Woodhouse 1997; Yoshizawa & Kennett 2002a) for the quantitative evaluation of the estimated phase speeds. The advantage of the use of this parameter is that it provides us with comprehensive information on the available frequency range and mode branches with quantitative estimates for quality of the measurements. Here, we define a new reliability parameter for multimode dispersion, which have been improved from the original one (Yoshizawa & Kennett 2002a).

First, we consider three seismograms: the observed seismogram  $u^{\text{obs}}(t)$ , the full synthetic seismogram  $u^{\text{syn}}(t)$ , and the synthetic seismogram of the *j*-th mode branch  $u_j^{\text{syn}}(t)$ . We now introduce a misfit seismogram between observed and full synthetic seismograms  $u^{\text{mis}}(t) = u^{\text{obs}}(t) - u^{\text{syn}}(t)$ , and a residual synthetic seismogram for *j*-th mode branch  $u_j^{\text{res}}(t) = u^{\text{syn}}(t) - u_j^{\text{syn}}(t)$ . Then, we calculate the corresponding spectrograms  $S^{\text{syn}}(\omega, t)$ ,  $S_j^{\text{syn}}(\omega, t)$ ,  $S^{\text{mis}}(\omega, t)$  and  $S_j^{\text{res}}(\omega, t)$  in the frequency–time domain. The spectrograms are derived from the power spectra of the seismograms with moving time windows.

Now, we consider two parameters; the relative waveform fit  $f(\omega, t)$  and the relative power  $p_j(\omega, t)$  for *j*-th mode branch (Fig. 5). The relative waveform fit  $f(\omega, t)$  is a parameter that quantifies how well

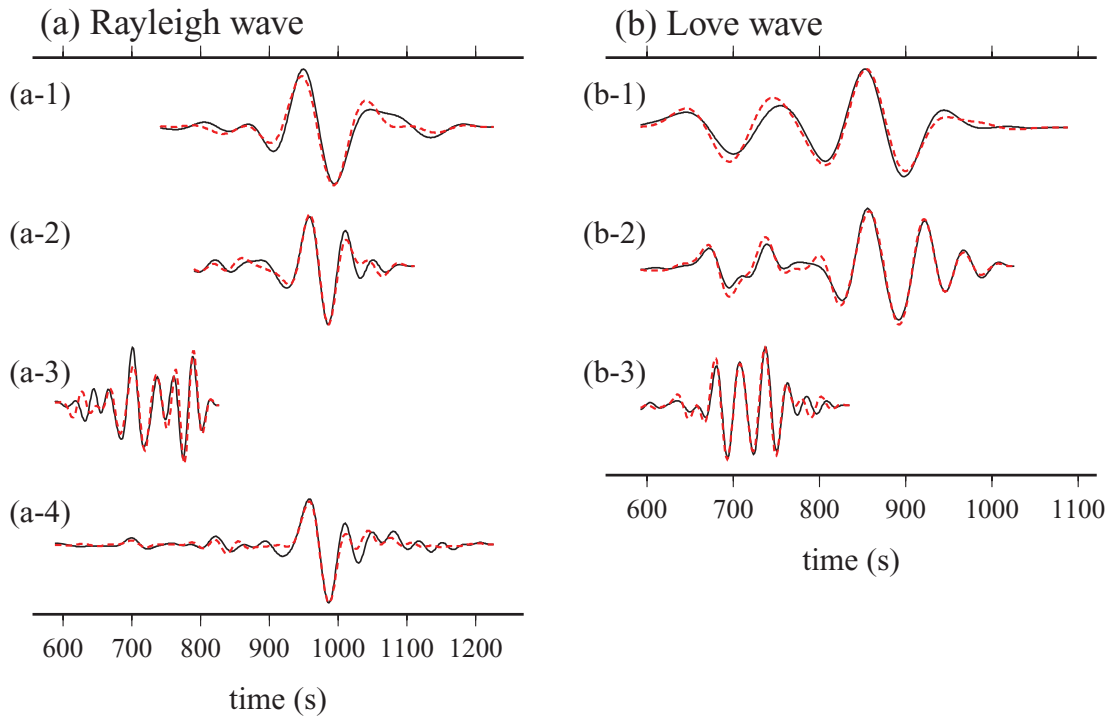


**Figure 3.** Examples of the results of waveform fitting with multiple time windows for two USArray stations from a seismic event in Chiapas, Mexico at 113 km depth on 2007 July 6. (a) Rayleigh waves (vertical component) for the station J13A, and (b) Love waves (transverse component) for the station J12A. Black solid lines are observed waveforms and red dashed lines synthetic waveforms. The time windows are determined from group speeds as given in Table 1. The frequency ranges are (a-1) 5–12 mHz, (a-2) 10–25 mHz, (a-3) 20–50 mHz, (a-4) 5–30 mHz, (b-1) 5–12 mHz, (b-2) 10–30 mHz and (b-3) 20–50 mHz.

**Table 1.** A summary of time windows used in this study. Group speeds are used to define the start and end time of each window. Multiple bandpass filters with specific frequency ranges are applied to each time window for appraisal of waveform misfit.  $T_s$  indicates that the start time of the window is determined from the  $S$ - or  $SS$ -wave arrival calculated from the AK135 model.

Window ID	Rayleigh wave			Love wave		
	Group speed ( $\text{km s}^{-1}$ )		Frequency range (mHz)	Group speed ( $\text{km s}^{-1}$ )		Frequency range (mHz)
	Min.	Max.		Min.	Max.	
1	2.9	4.8	5 – 10 7 – 12	3.3	$T_s$	5 – 10 7 – 12
2	3.2	4.5	10 – 18 15 – 25	3.5	$T_s$	10 – 20 15 – 30
3	4.3	$T_s$	20 – 33 25 – 50	4.3	$T_s$	20 – 33 25 – 50
4	2.9	$T_s$	5 – 12 10 – 20 15 – 30			

the observed waveforms are fit by the synthetic, and is defined as,  $f(\omega, t) = [\exp\{-S^{\text{mis}}(\omega, t)/S^{\text{syn}}(\omega, t)\}]^3$ . We use the third power of the exponential term to make the parameter  $f$  more sensitive to small differences in the waveform misfit. The relative power  $p_j(\omega, t)$  of the  $j$ -th mode represents the relative contribution of the amplitude of the  $j$ -th mode in the full synthetic seismogram, and is defined as,  $p_j(\omega, t) = \exp\{-S_j^{\text{res}}(\omega, t)/S_j^{\text{syn}}(\omega, t)\}$ .

To obtain the reliability parameter  $r_j(\omega)$  as a function of frequency, and across a time window  $T_w$ , the relative waveform fit and the relative power of each mode are then multiplied and integrated over the time window  $T_w$  at frequency  $\omega$  as,  $r_j(\omega) = n_t \int_{T_w} p_j(\omega, t) f(\omega, t) dt$ , where  $n_t$  is a normalization factor of the reliability. The maximum value of the reliability varies depending on the time span for which waveforms are matched well and a par-

ticular mode is sufficiently energetic. To simplify the comparisons among the estimated reliability parameters, we employ  $n_t$  such that the reliability becomes 1.0 when we achieve a perfect waveform fit and relative power (i.e. both  $f$  and  $p_j$  are 1.0) for a 10 s time window.

An example of the estimated dispersion curves and the corresponding reliability parameters is displayed in Fig. 6. We choose the frequency range of the dispersion curves of each mode for which the reliability parameter is higher than a threshold value. The numbers of acceptable measurements of multimode phase speeds will vary depending on the choice of the threshold values for the total waveform misfit  $\Phi$  and the reliability parameter  $r_j$ . Through extensive tests using different criteria for the threshold values, we have determined an appropriate combination of thresholds that

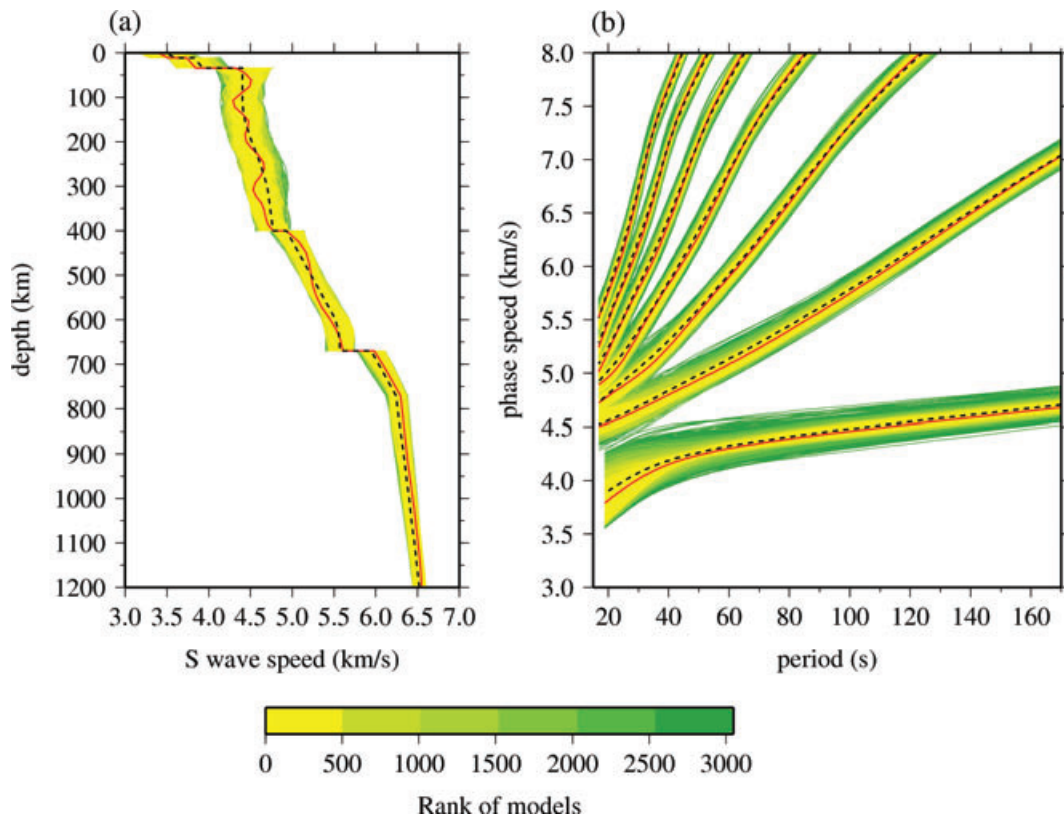


**Figure 4.** (a) Path-specific 1-D shear wave speed profiles derived from the global parameter search with the Neighbourhood Algorithm (NA) for the Love waves in Figs 3(b), and (b) corresponding dispersion curves estimated from the 1-D models in (a). All the 3050 models constructed with the NA are ranked in order of the smaller misfit, and are plotted with colours varying from green (larger misfit) to yellow (smaller misfit). The red line is the best-fit model, and the black dashed line is the reference model.

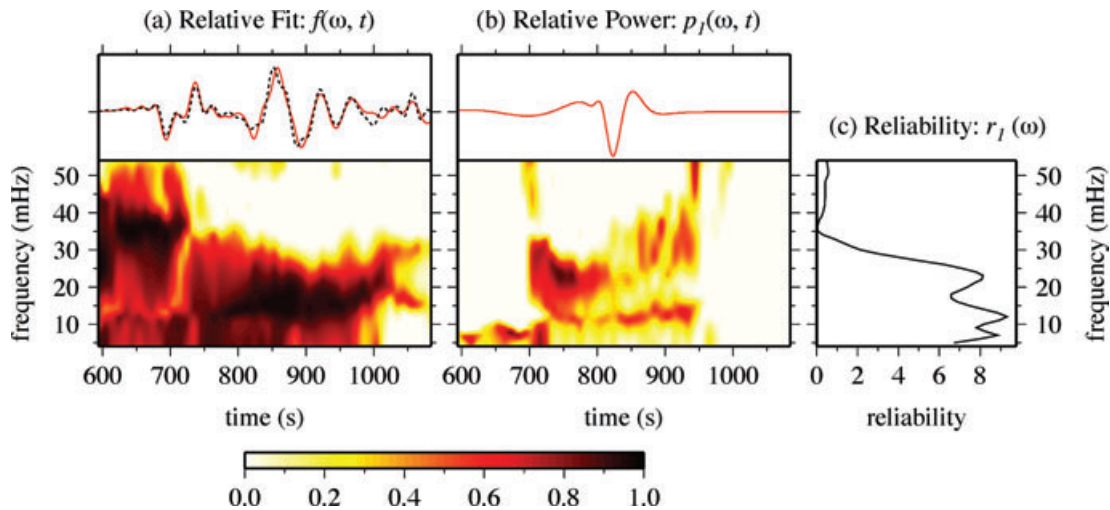


**Figure 5.** (a) Full synthetic (red line) and observed (black dashed line) seismograms of Love waves in Fig. 3(b), and the relative waveform fit  $f(\omega, t)$  in the frequency–time domain. (b) A mode branch seismogram for the first higher mode of Love wave, and the relative power of the mode  $p_j(\omega, t)$  in the frequency–time domain. (c) Reliability parameter  $r_j(\omega)$  for the first higher mode calculated from (a) and (b).

provides us with a reasonably good waveform fit and reliable dispersion curves. The final choice of the combinations of threshold values is summarized in Table 2. The thresholds for the reliability parameters vary depending on the waveform misfit  $\Phi$  which represents the overall quality of waveform matching. In the example of Fig. 6, we set the threshold of reliability to 8.0 for the fundamental mode and 2.0 for the higher modes.

### 3 APPLICATION TO REGIONAL PATHS IN NORTH AMERICA

#### 3.1 Data set of seismograms and pre-processing

In this study, we used three-component long-period seismograms that are available from the IRIS Data Management Center, for

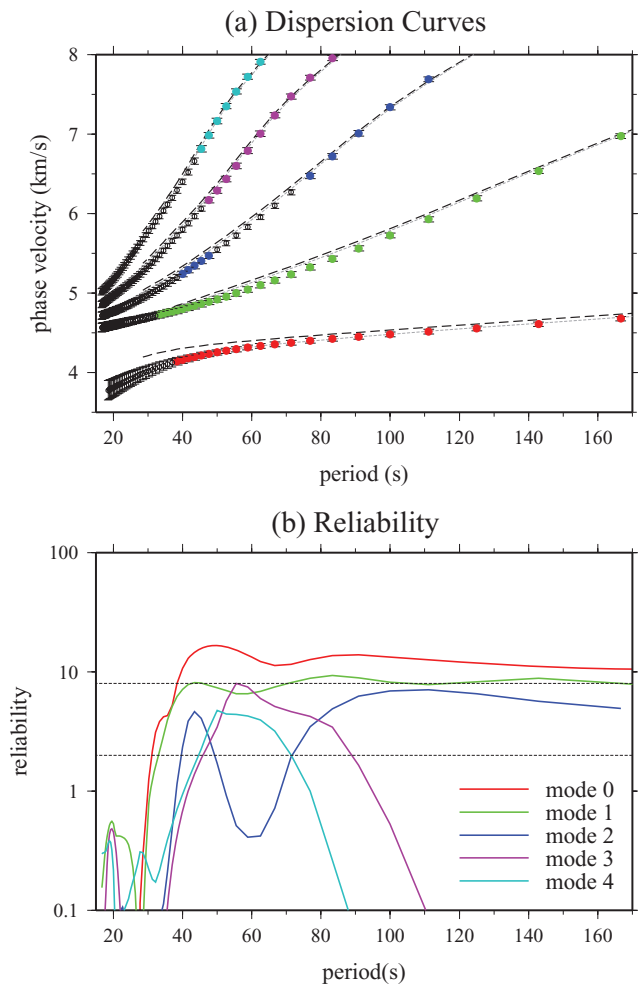


**Figure 6.** (a) An example of estimated dispersion curves for Love waves in Fig. 3 (b) up to the fourth higher mode, and (b) the corresponding reliability parameters as a function of period. The coloured dots in (a) indicate the selected measurements with higher reliability than the threshold values. In this example, the threshold for the reliability parameter for the fundamental mode is set to 8.0 and that for the higher modes is 2.0.

**Table 2.** Threshold values of the reliability  $r_j$  and normalized radiation amplitude  $\bar{A}_j$  of each mode as a function of specific ranges of the total waveform misfit  $\Phi$ . If the waveform misfit is greater than 0.03, the dispersion curves for none of the modes are used since no portion of synthetic and observed waveforms could be matched at a satisfactory level.

Waveform misfit $\Phi$	Minimum reliability		Minimum radiation $\bar{A}_j$
	$r_j(j = 0)$	$r_j(j \geq 1)$	
0.00 – 0.01	8.0	2.0	0.5
0.01 – 0.02	9.0	2.5	0.6
0.02 – 0.03	10.0	3.0	0.7

seismic events from 2000 January to 2008 April. The locations of stations and events are plotted in Fig. 7. The centroid moment tensors for the synthetic calculations are taken from the Global CMT catalog (Dziewonski *et al.* 1981; Ekström *et al.* 2005). Prior to the waveform analysis, the instrument response of the original seismograms is deconvolved to obtain ground displacement, and horizontal components are rotated to the radial and transverse di-

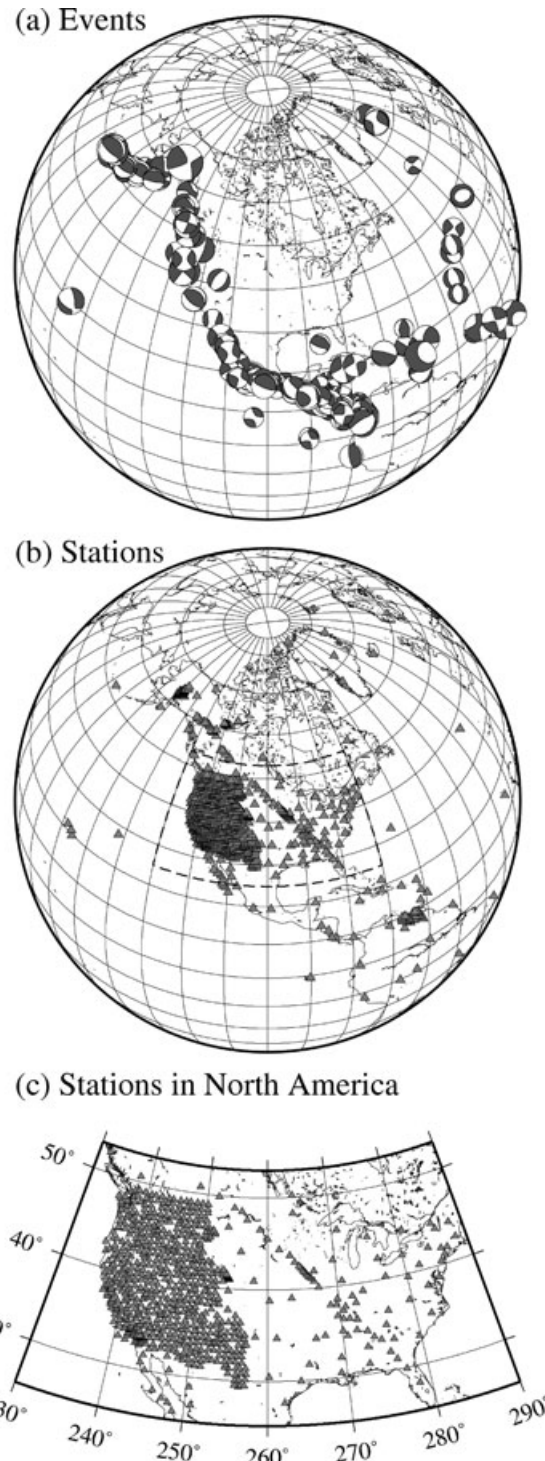


**Figure 7.** The distribution of (a) seismic events, (b) stations used in this study and (c) stations in North America.

rections. Waveforms with low signal-to-noise ratio are discarded prior to the waveform inversion.

To minimize the large uncertainties of the phase speed measurements in the nodal direction of surface wave radiation, we also quantitatively evaluate the radiation patterns of each mode at the seismic source location using the Global CMT. If a station is found to be located in the nodal direction of surface wave radiation for

a particular mode, we do not use it. In this study, we consider the normalized radiated amplitude  $A_j(\zeta, \omega)/A_j^{\max}(\omega)$ , where  $A_j(\zeta, \omega)$  is the amplitude of the  $j$ -th mode at angular frequency  $\omega$  in the azimuth  $\zeta$  from the source, and  $A_j^{\max}(\omega)$  is the maximum amplitude of the surface wave radiation pattern for the  $j$ -th mode at frequency  $\omega$ . Then, we consider the average of the normalized radiation  $\bar{A}_j(\zeta)$  over a frequency range. The nodal direction is defined as the azimuth  $\zeta$  for which the average normalized amplitude  $\bar{A}_j(\zeta)$  is less than the threshold values given in Table 2.

### 3.2 Starting model and scaling relation

We perform the waveform inversion using not only the reference model described in Section 2.1, but also other four different starting models as displayed in Fig. 8. These additional starting models contain  $\pm 1.5$  per cent and  $\pm 3.0$  per cent perturbations from the original reference model in the uppermost mantle. For each waveform inversion initiated with a single starting model, we create 3050 models using the NA. Thus, with five starting models, we evaluate 15 250 models in total for each seismogram. This process allows us to minimize unwanted results due to phase cycle skip, which could happen when a chosen initial model is too far from the actual Earth structure.

In this study, we use the model that provides the best waveform fit to estimate the phase speeds. In most cases, the best fit model derived from the NA is very close to the average of the ensemble of models, and the first several hundred models tend to converge on nearly identical dispersion curves.

To simplify the representation of wavenumber perturbation in eq. (2), we consider only the  $S$ -wave speed perturbation as an in-

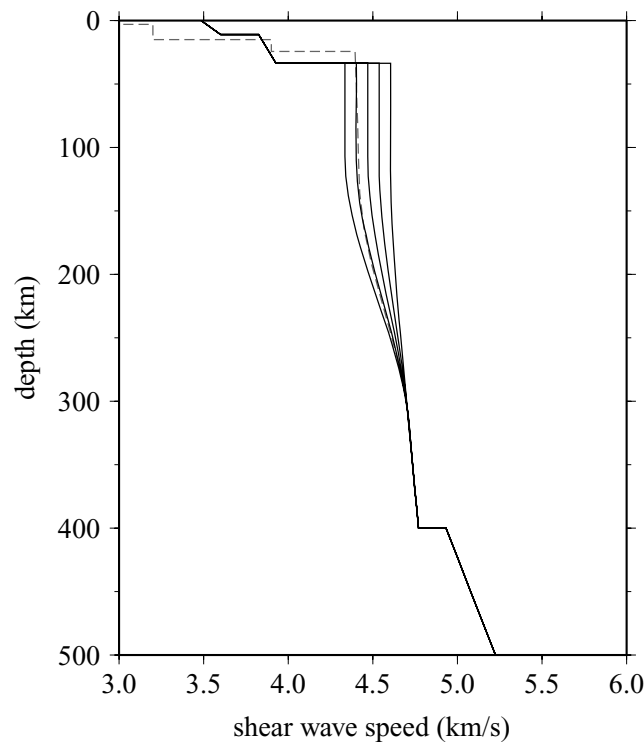


**Figure 8.** Five starting models (black lines) used to initiate the non-linear waveform inversions for examples in Fig. 3. The grey dashed line is PREM with a smoothed discontinuity at 220 km depth.

dependent variable, and use scaling parameters for  $P$ -wave speed and density;  $(m_\alpha, m_\rho) = (d \ln \alpha / d \ln \beta, d \ln \rho / d \ln \beta)$ . There are many ways for scaling of these parameters depending on the results from mineral physics as well as seismic and geodynamic modelling (e.g. Montagner & Anderson 1989; Masters *et al.* 2000; Deschamps *et al.* 2001; Resovsky & Trampert 2003). In this study, we employed a linearly varying scaling relation for  $P$ -wave speed;  $m_\alpha = 0.8$  at the surface and  $m_\alpha = 0.3$  at the CMB. For the density scaling, we use  $m_\rho = 0.4$ . It should be noted that the choice of the scaling parameters has only secondary effects, and the other choices of these parameters do not alter the results of our phase speed measurements.

### 3.3 Quality control of the measured dispersion curves

The reliability parameters and waveform misfit functions are useful diagnostic parameters for the automated evaluation of the estimated multimode dispersion curves from waveform fitting. However, some outliers can still be included in the measurements derived from a large number of seismograms. There are several factors that could cause outliers in the measurements, such as possible errors in the source locations, origin time and centroid moment tensors, as well as the effects of phase cycle skips.

To detect outliers included in the ensemble of estimated phase speeds automatically, we perform a statistical outlier detection using the Grubbs' Test (Grubbs 1969). The Grubbs' Test detects a single outlier in a normally distributed univariate data set. For the extreme value  $x_n$  (maximum or minimum) in the sample, we estimate the statistic  $T_n = |x_n - \bar{x}|/s$ , where  $\bar{x}$  and  $s$  are the sample mean and standard deviation, respectively. If  $T_n$  is larger than a critical value that is derived from the  $t$ -distribution and the number of samples  $n$ , the datum is regarded as an outlier and is removed from the sample. The process is repeated until no outlier is found in the rest of the sample.

As a first step of detecting outliers, we consider a corridor of surface wave paths for a group of stations and events located in a certain area, which is defined as a circular region with a radius,  $L \sin \Delta$ , around the reference station or event.  $\Delta$  is the epicentral distance between the reference station and event; we use  $L = 2.5^\circ$  in this study.

For the dispersion curves derived from the group of paths (or a surface wave corridor), we conduct the Grubbs' Test to detect outliers in the ensemble of measured phase speeds at a certain frequency. Repeating this process for the entire frequency range, we can estimate the confidence interval that provides a proper range of measurements around the average dispersion curve, and eventually allows us to detect a probable outlier in an automated manner.

An example of surface wave corridor is shown in Fig. 9(a), and the measured phase speeds for all the paths are plotted in Fig. 9(b) with the colour indicating the reliability of each of the measured phase speeds. The weighted average of the measurements is shown with the yellow dashed line. The reliability parameter is used as a weight on each measurement when we calculate the weighted average of phase speeds. Fig. 9(c) is a histogram of the phase speeds at a period of 125 s in Fig. 9(b), with a theoretical curve of the normal distribution. The two red dashed lines in Figs 9(b) and (c) represent the 99 per cent confidence interval. The measured phase speeds lying outside of these two red lines can be regarded as outliers, and are removed from our data set.

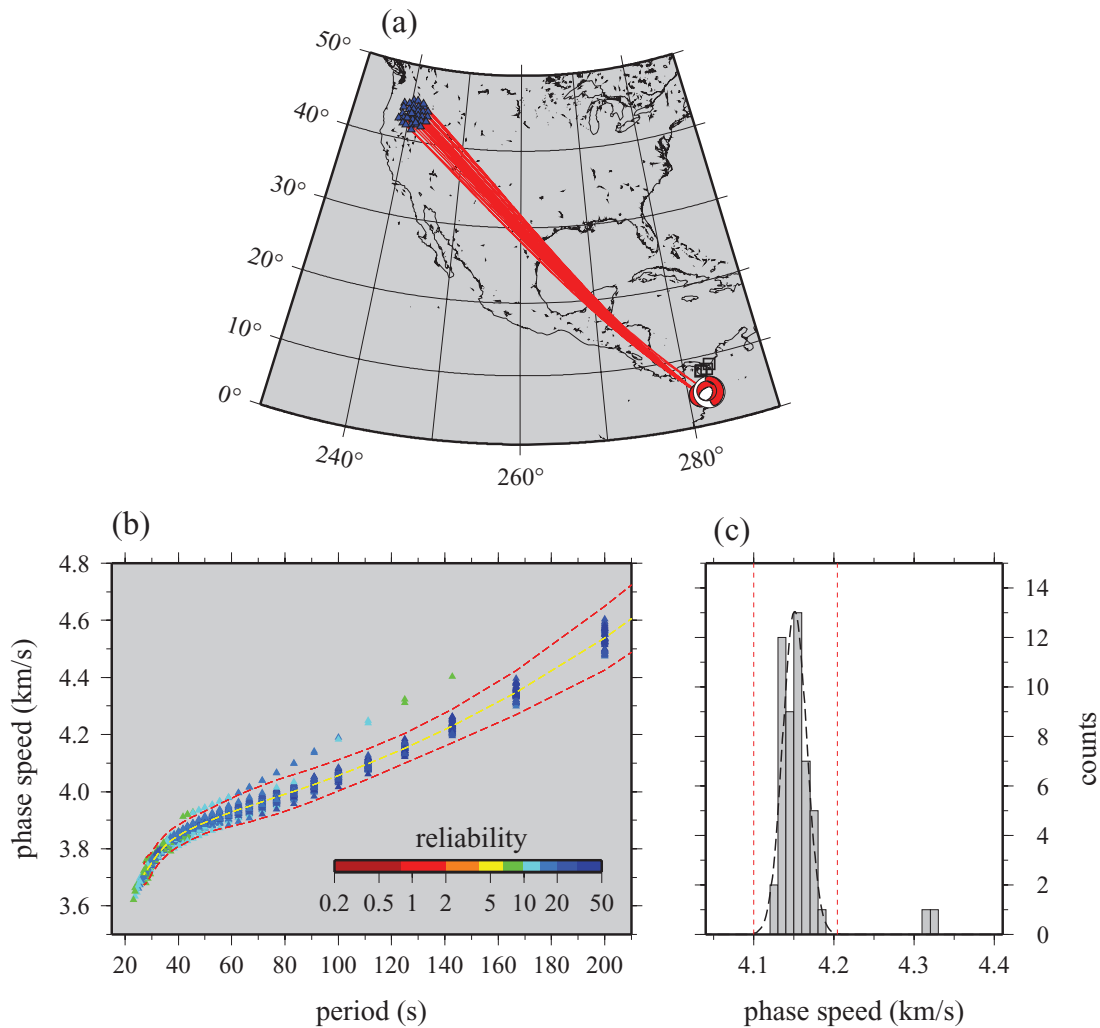


**Figure 9.** (a) An example of a surface-wave corridor (a group of paths) between groups of stations and events. (b) Measured phase speeds for the fundamental-mode Rayleigh waves along the paths in (a). The yellow dashed line is the weighted average of observed dispersion curves and the red dashed lines indicate the 99 per cent confidence interval. (c) A histogram of the measured phase speed at 125 s period in (b), with a theoretical normal distribution.

Such statistical outlier detection can be used only for surface wave corridors including at least five or more paths. If there are only a few paths in the corridor, we cannot perform this type of statistical analysis, and we include such measurements just relying on the reliability parameter. It should be noted that, in many cases, the reliability parameter itself provides an insight into possible outlying measurements. This can be seen in Fig. 9(b), which shows that outlying phase speeds have relatively smaller reliability close to the threshold value in Table 2, whereas the other phase speeds within the 99 per cent confidence level have much higher reliability. In this study, about 72–79 per cent of dispersion curves, depending on components, are checked by the Grubbs' Test, while the remaining ones are selected through the reliability analysis alone.

### 3.4 Data set of multimode phase speeds

We have analysed over 66 000 vertical seismograms and 52 000 horizontal seismograms for both radial and transverse components

from 244 events (Fig. 7). The numbers of measurements of multimode phase speeds, which have successfully passed all the required criteria as described in the preceding sections, are summarized in Fig. 10. We have gathered more than 20 000 measurements for the fundamental-mode Rayleigh waves (vertical component) over a wide frequency range, and over 10 000 for the fundamental-mode Love waves as well as the higher mode Rayleigh waves, and over 3000 for the higher mode Love waves.

We display two examples of path coverage maps in Fig. 11; one is the fundamental mode Rayleigh wave at 76.9 s, which includes 23 089 paths, the largest number of all the modes and frequencies, and the other is the second Love-wave mode with 3714 paths. In both cases, we achieve good coverage across North America, even though the ray path density is certainly different between these two extreme cases.

The majority of the phase speed data are derived from the transportable stations of USArray and the locations of seismic events are biased to western North America (Fig. 7). Therefore, the ray path density is much higher in the western United States, particularly

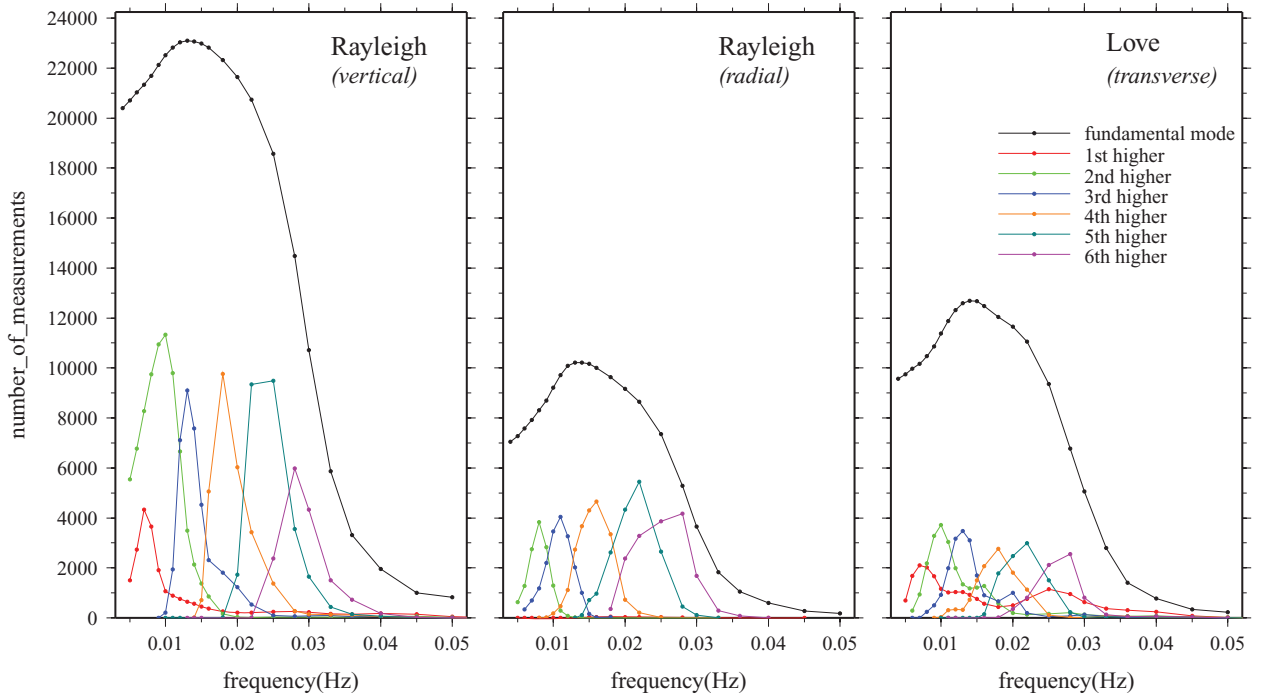


**Figure 10.** Numbers of measurements of multimode phase speeds for vertical-component Rayleigh waves (left-hand panel), radial-component Rayleigh waves (middle panel) and Love waves (right-hand panel), as a function of period.

in the NW–SE directions, whereas the paths in the northeastern United States are relatively sparse. This situation will improve with the future deployment of USArray to cover the central and eastern United States.

#### 4 PHASE SPEED MAPS OF NORTH AMERICA

Using the large number of the measurements of multimode phase dispersion, we perform inversions for multimode phase speed maps employing the method developed by Yoshizawa & Kennett (2004). The finite-frequency propagation effects of surface waves are incorporated using the influence zone of surface wave paths (Yoshizawa & Kennett 2002b).

##### 4.1 Method of finite-frequency phase speed mapping

The method of our finite-frequency phase speed tomography has been described in detail by Yoshizawa & Kennett (2004). Here, we briefly summarize the method for the phase speed mapping incorporating approximate effects of finite-frequency of surface waves. In a ray-centred coordinate system  $(s, n)$ , where  $s$  is a length along a path and  $n$  is along an axis perpendicular to the path, the linearized relation of a phase perturbation of seismograms  $\delta\psi$  and a structural phase speed perturbation  $\delta c$  can be written as

$$\delta\psi = \int_{\text{path}} ds \int_{\text{width}} dn \mathcal{K}_\psi(s, n) \frac{\delta c(s, n)}{c_0}, \quad (3)$$

where  $\mathcal{K}_\psi$  is the 2-D sensitivity kernel for phase speed structures, and  $\delta c/c_0$  is a fractional phase speed perturbation to be determined through the inversion. The phase perturbation of the observed seismogram  $\delta\psi^{\text{obs}}$  can be related to the observed phase speed perturbation  $\langle \delta c \rangle^{\text{obs}}$  as,  $\delta\psi^{\text{obs}} = -k_0 \Delta \langle \delta c \rangle^{\text{obs}} / c_0$ , where  $k_0$  and  $c_0$  are the

wavenumber and phase speed for the reference model, respectively, and  $\Delta$  is the distance along a path,

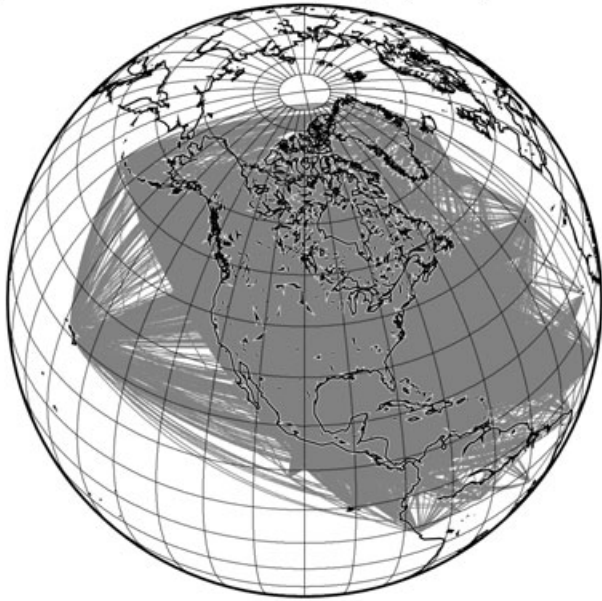
An example of the sensitivity kernels used in this study is displayed in Fig. 12. The finite-width kernels are derived from the influence zone of surface wave paths, which has been identified as approximately one-third of the width of the first Fresnel zone in which surface waves are coherent in phase (Yoshizawa & Kennett 2002b). The width of the influence zone becomes wider at longer periods because the absolute phase speed is faster and its wavelength becomes longer. The kernel in Fig. 12 is simplified compared to the more rigorous finite-frequency kernels based on Born theory (e.g. Zhou *et al.* 2004; Yoshizawa & Kennett 2005). However, such kernels based on the influence zone can be a reasonable approximation of the Born sensitivity kernels (e.g. Levshin *et al.* 2005).

The linearized equation (3) can be written in a generalized form,  $\mathbf{d} = \mathbf{G}\mathbf{m}$ , where  $\mathbf{d}$  is a data vector,  $\mathbf{G}$  the kernel matrix and  $\mathbf{m}$  a vector of model parameters  $m_j (j = 1, 2, \dots, N)$ , where  $N$  is the number of model parameters. To expand the phase speed perturbation on a sphere, we employ spherical B-spline functions  $\mathcal{F}_j(\theta, \phi)$  (Wang & Dahlen 1995) which are defined at the rectangular geographical grids,

$$\frac{\delta c(\theta, \phi)}{c_0} = \sum_{j=1}^N m_j \mathcal{F}_j(\theta, \phi), \quad (4)$$

where the model parameter  $m_j$  is the coefficient for the  $j$ -th basis function  $\mathcal{F}_j$ . The grid (or knot) interval used in this study varies depending on the numbers of paths; we used  $1.5^\circ$  for models with more than 10 000 paths,  $2.0^\circ$  for over 5000 paths,  $3.0^\circ$  for over 3000 paths and  $4.0^\circ$  for over 1500 paths. The total number of model parameters  $N$  depends on the path coverage and knot interval for each mode and frequency, and it varies in a range between 1000 and 3200.

## (a) fundamental mode; Rayleigh (76.9s)



## (b) 2nd higher mode; Love (100s)



**Figure 11.** Path coverage for (a) the fundamental-mode Rayleigh wave at 76.9 s and (b) the second higher mode Love wave at 100 s.

The linear equation is solved with a damped least-squares scheme using the LSQR algorithm (Paige & Saunders 1982), and we use the reliability parameters as a weight on each phase speed datum.

#### 4.2 Horizontal resolution

We performed checkerboard resolution tests with a variety of sizes of checkerboard patterns, to assess visually the horizontal resolution of our model. In our checkerboard test, synthetic data are generated incorporating the finite-frequency effects using the influence zone, and then the synthetic data are inverted using the same damping as

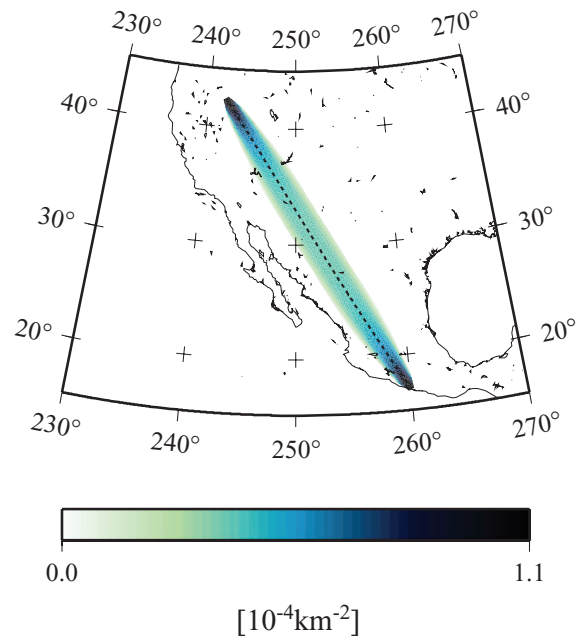


**Figure 12.** Finite-width sensitivity kernels for the fundamental-mode Rayleigh wave at 100 s, based on the influence zone of Yoshizawa & Kennett (2002b, 2004).

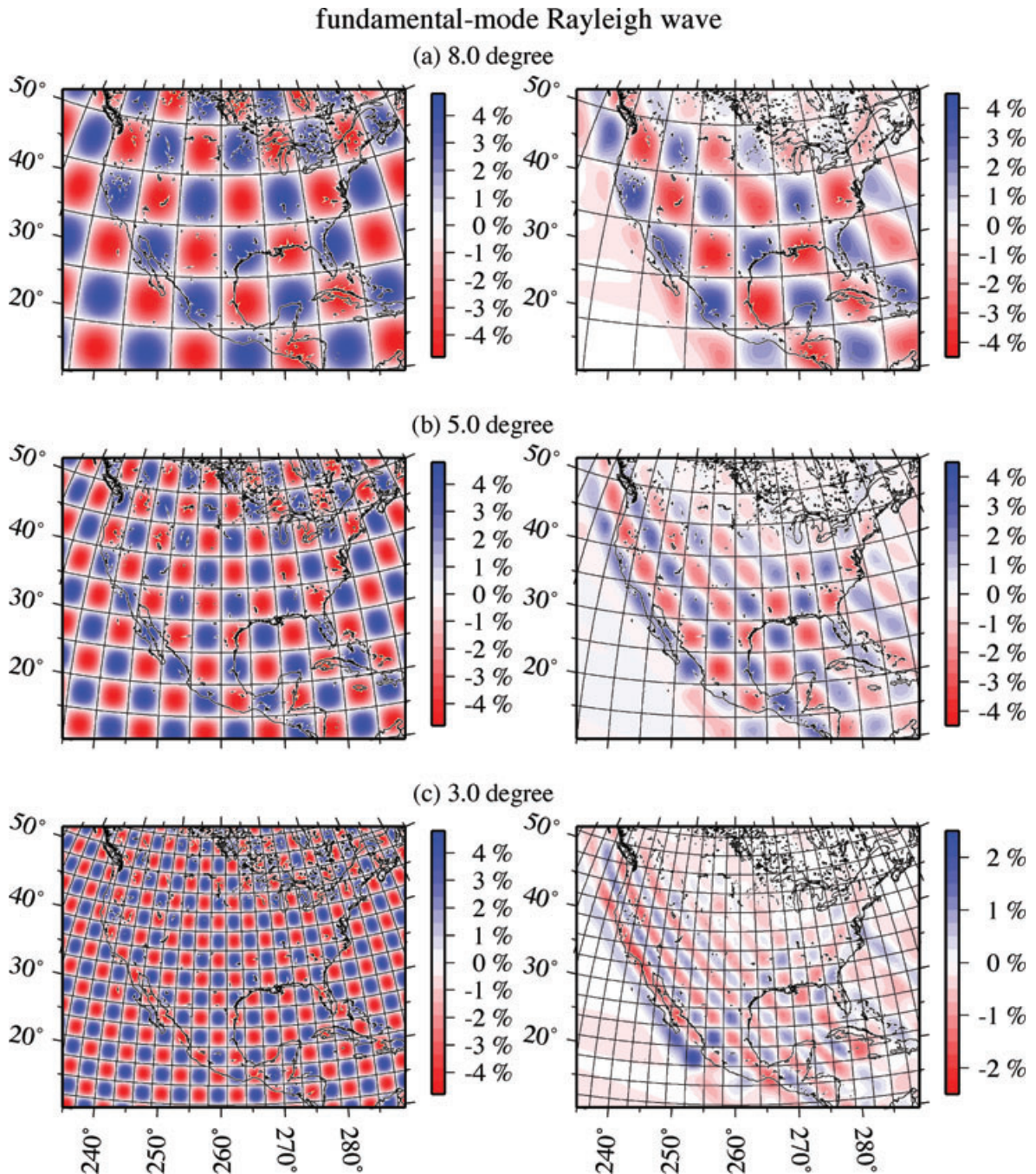
in the real data inversion. Weighing factors that depend on measurement reliability for each path are also applied.

Fig. 13 displays the input and recovered checkerboard models for the fundamental-mode Rayleigh waves at 76.9 s, and Fig. 14 the second higher mode Love waves at 100.0 s, with different sizes of cell patterns. In all cases, the western and southern regions of North America are retrieved fairly well at large scales. Checkerboard patterns over 5-degree cells for the fundamental mode and 8-degree cells for the higher modes are generally retrieved well even with the smaller data set of other modes and frequencies. We achieve fairly uniform resolution with horizontal scales about 400–500 km for the fundamental mode in most regions of the United States, Mexico and the Gulf of Mexico, but we cannot resolve the Pacific Ocean and the northeastern region of North America, particularly in eastern Canada, where we do not have enough crossing paths.

Because a very large data set for the fundamental-mode Rayleigh waves is available, we resolve smaller scale heterogeneity with 3° or less as shown in Fig. 13(c). For smaller scale patterns, the smearing effects in the NW–SE direction becomes apparent, particularly in the western United States. This is mainly because the current ray coverage is biased towards the western half of the North American continent, due to the uneven distribution of seismic events and stations (Fig. 7). Such biased coverage can be remedied as the USArray stations move towards the centre and eastern United States, eventually covering the entire United States uniformly.

#### 4.3 Multimode phase speed maps of North America

We display a topographic map of North America with some major geological features in Fig. 15, and examples of the phase speed maps for the fundamental mode in Fig. 16 and for the higher modes in Fig. 17. The corresponding vertical sensitivity kernels for shear wave speed are shown in Fig. 18. The achieved variance reductions of the phase speed models are about 52–88 per cent for the



**Figure 13.** Results of checkerboard resolution tests for the fundamental-mode Rayleigh wave at 76.9 s using cellular patterns with (a) 8.0°, (b) 5.0° and (c) 3.0°. Input models are displayed on the left-hand panels and output models on the right-hand panels.

fundamental modes and about 51–71 per cent for higher modes, depending on frequency.

For comparisons of multimode dispersion maps, we display the global phase speed models of the fundamental-mode surface waves with enhanced resolution in North America by Nettles (2005) in Fig. 19, and the isotropic part of the global phase speed maps of Visser *et al.* (2008) in Fig. 20, focusing on the North America region. To compare directly with the phase speed maps in Figs 16 and 17, the models in Figs 19 and 20 are plotted as a perturbation from an average phase speed estimated from our regional data set in North America.

#### 4.3.1 Fundamental-mode models

In the fundamental mode models in Fig. 16, a strong velocity contrast between the western and central United States across the eastern margin of the Rocky Mountains is clearly imaged. Such a feature of North America has been common in tomography models of North America from both global scale (e.g. Marone *et al.* 2007; Nettles & Dziewonski 2008) and regional-scale studies (e.g. van der Lee & Frederiksen 2005; Bedle & van der Lee 2009). Large-scale heterogeneity patterns of our model are fairly consistent with the North American phase speed model by Nettles (2005) in Fig. 19,

## 2nd higher-mode Love wave

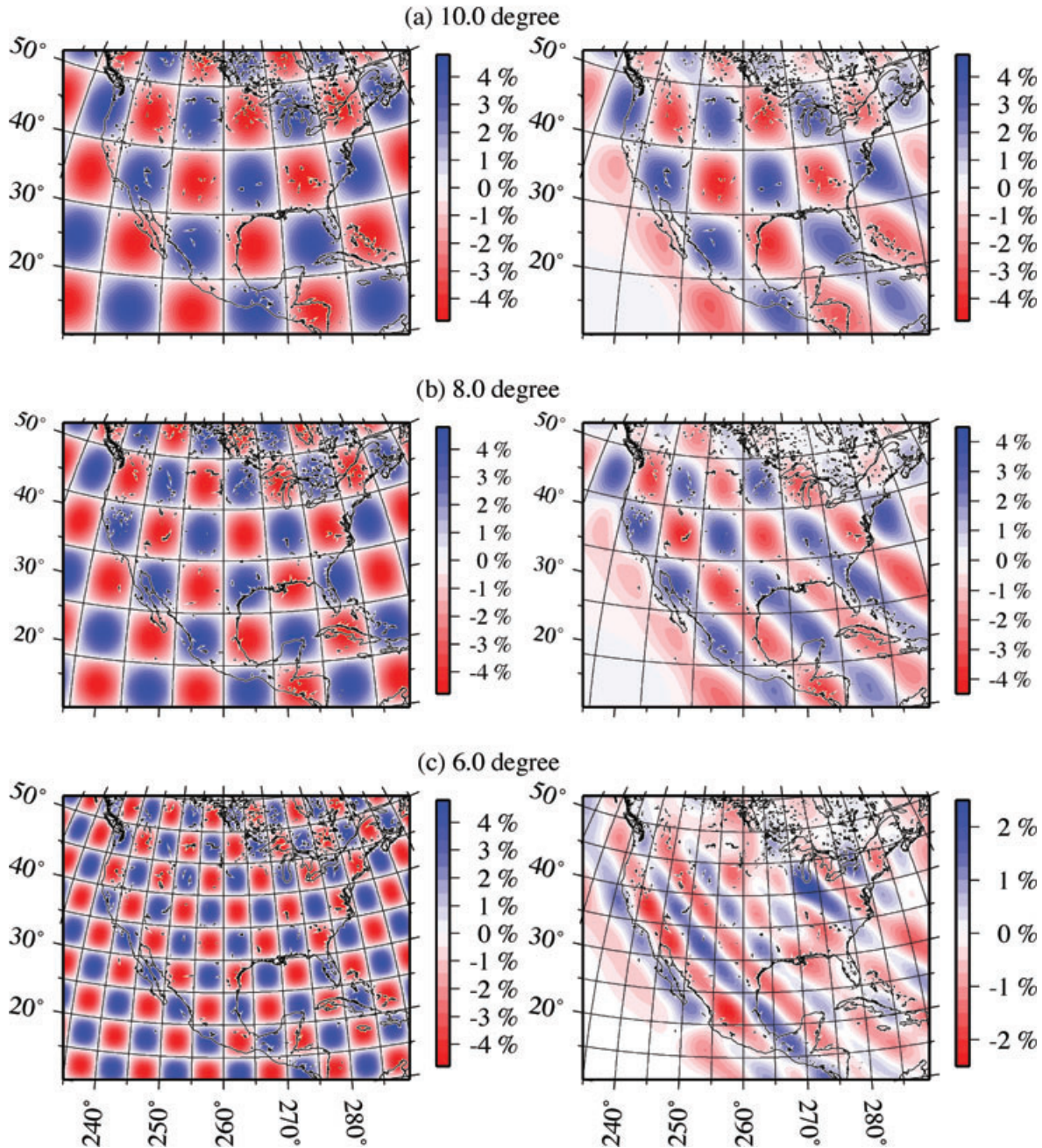


**Figure 14.** Same as Fig. 13, but for the second higher mode Love wave at 100 s, using cellular patterns with (a) 10.0°, (b) 8.0° and (c) 6.0°.

though our regional models include richer information on localized heterogeneity in the upper mantle compared to the global-scale study.

In the Rayleigh-wave model at 62.5 s (Fig. 16c), we see some conspicuous slow anomalies in the Great Basin. Also a linear, slow anomaly along the Rio Grande Rift zone can be identified. Similar slow anomalies are also found in the fundamental-mode Rayleigh-wave model by Nettles (2005) in Fig. 19(c). These anomalies are not very clear in the Love-wave models (Figs 16a and b and Figs 19a and b), indicating possible radial anisotropy beneath the tectonically active regions in the western United States.

Slow anomalies are found in the west of the Cascade Range in western North America in Figs 16 and 17. This region locates at the western edge of the well-resolved area of our model, due to the limited numbers of crossing paths in the Pacific Ocean, resulting in low horizontal resolution of small-scale heterogeneity (e.g. Fig. 13c). Thus, this region is likely to be affected by uncertainties in the measurements and biased path coverage, and we are unable to discuss the detailed local structure in the Pacific.

Fast anomalies in the central and eastern parts of North America are prominent in the fundamental mode models of both Love and Rayleigh waves which are sensitive to structure at depths



**Figure 15.** Topographic map of North America. Plate boundaries are taken from Bird (2003). ATL: Atlantic Ocean, APM: Appalachian Mountains, GB: Great Basin, GC: Gulf of California, JdF: Juan de Fuca Plate, MTJ: Mendocino Triple Junction, PAC: Pacific Plate, RGR: Rio Grande Rift, SN: Sierra Nevada, SRP: Snake River Plains and YS: Yellow Stone Hotspot.

around 100 km (Figs 16b,c and Figs 18a,b), reflecting the fast continental lithosphere, whereas such features are weaker in the models that sample shallower or deeper parts of the mantle (Figs 16a and d).

The structure of the Gulf of Mexico is also clearly mapped. In particular, a prominent fast phase speed anomaly is found beneath the western half of the Gulf of Mexico in the fundamental mode Love-wave models (Figs 16a and b), which have the highest sensitivity at depths just below the Moho discontinuity (Fig. 18a). Such fast anomalies are found in both the Atlantic and the Gulf of Mexico in the Love-wave model at 62.5 s reflecting the oceanic lithosphere with a thin crust. A similar fast anomaly can be seen in Rayleigh-wave model at 62.5 s (Fig. 16c) beneath the Atlantic, but is weaker in the Gulf of Mexico. Similar features of fast anomalies in the Gulf of Mexico and Atlantic are also seen in the large-scale model of Nettles (2005) in Figs 19(a) and (c). This is likely to indicate differences in the thickness of the oceanic lithosphere beneath these oceanic areas, suggesting thinner lithosphere beneath the Gulf of Mexico.

#### 4.3.2 Higher mode models

Higher mode models in Fig. 17 show somewhat smaller perturbations of phase speeds. Despite intrinsic differences in the horizontal resolution and the data sets, we are able to see common features in large-scale heterogeneity distribution in our regional higher mode models (Fig. 17) and Visser's global model (Fig. 20). For example, in the second higher mode Love-wave models (Figs 17a and

20a), there is a prominent fast anomaly extending from northwest to southeast in the middle of North America and a slow anomaly from Arizona to the Gulf of California.

The higher modes sample the mantle structure in a very different way from the fundamental mode (Figs 18c and d). The higher mode Love-wave models in Figs 17(a)–(c) have the largest sensitivity in the mantle transition zone (second higher mode) or the lower mantle (third and fifth higher modes). Also, these modes sample the upper mantle with a similar sensitivity over a wide depth range in the upper mantle (Fig. 18c). These higher mode Love-wave models share similar patterns of fast and slow anomalies. This fact indicates that the majority of the common heterogeneity patterns in these models may come from the upper mantle to which all of the modes have a similar sensitivity, and thus we may infer a weak heterogeneity in the lower mantle to which the third and fifth higher modes have the peak sensitivity.

It should be noted that the higher mode Love-wave models in Figs 17(a)–(c) display a fast anomaly in the western United States, which is consistent with the ongoing subduction of the Juan de Fuca plate as well as a fragment of earlier subducted Farallon plates reported by some other studies. (e.g. van der Lee & Nolet 1997; Burdick *et al.* 2008; Sigloch *et al.* 2008).

The higher modes of Rayleigh waves in Figs 17(d)–(f) show similar patterns of heterogeneity to those of the fundamental mode Rayleigh wave, although the maximum perturbation is weaker in the higher mode models. Global models by Visser in Figs 20(d)–(f) also suggest such a characteristic of the Rayleigh-wave models. These higher Rayleigh modes have the greatest sensitivity in the structure in the uppermost mantle above 150 km with

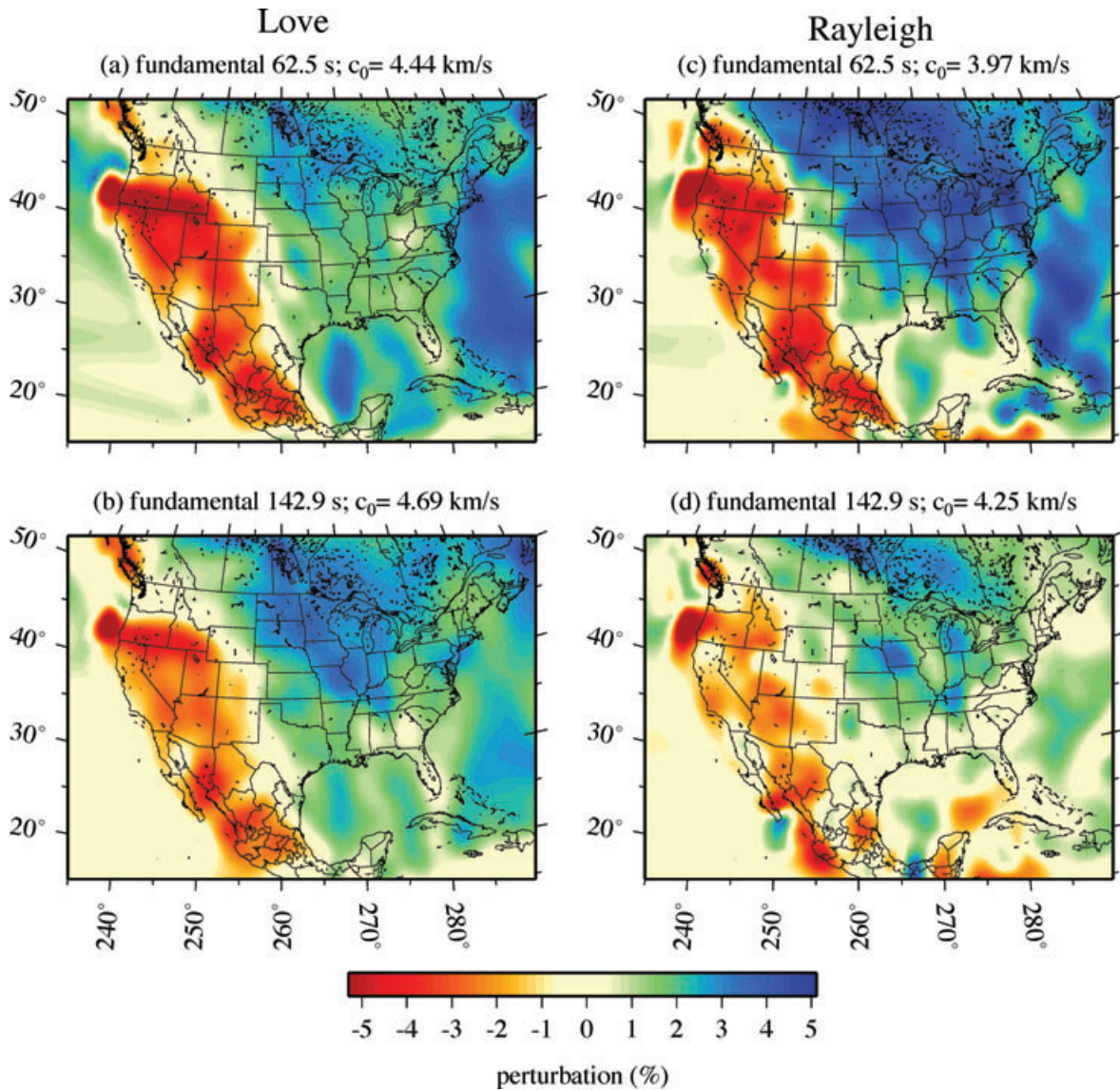


**Figure 16.** Fundamental-mode phase speed maps of (a) Love wave at 62.5 s, (b) Love wave at 142.9 s, (c) Rayleigh wave at 62.5 s and (d) Rayleigh wave at 142.9 s.

secondary peaks of sensitivity to the deeper part of the upper mantle below 300 km (Fig. 18d). Since the sensitivities of these higher mode Rayleigh waves to the shear wave structure share a common feature with only slight differences in the depth of peak sensitivity, the phase speed maps tend to display common characteristics.

The interpretation of the higher mode phase speed maps is generally not straightforward, because their vertical sensitivity to the shear waves structure is much more complicated than the fundamental mode (Fig. 1). Thus, the more detailed discussions on the mantle structure should be pursued based on the shear wave models that can be obtained from the multimode dispersion maps. Combining these high-resolution multimode phase speed models would allow us to map the detailed image of not only heterogeneity but also radial anisotropy in a wide depth range of the mantle, which can be derived from the simultaneous inversions of Love and Rayleigh waves.

## 5 DISCUSSION AND CONCLUSIONS

We have developed a fully automated method of obtaining multimode phase speed measurements, based on the non-linear waveform inversion of Yoshizawa & Kennett (2002a). Several empirical parameters, such as the reliability parameter and the waveform misfit, allow us to select automatically the reliable dispersion measurements derived from the non-linear waveform fitting. The supplementary process of automatic outlier detection based on the statistical approach using the Grubbs' Test enables us to refine the measured data set of the multimode phase speeds. Although the automated method is based on several subjective parameters, slight differences in chosen threshold values do not have significant influence on the final results of our phase speed measurements.

Despite the use of the fully non-linear approach with the NA as a global optimizer, our method of non-linear waveform fitting is

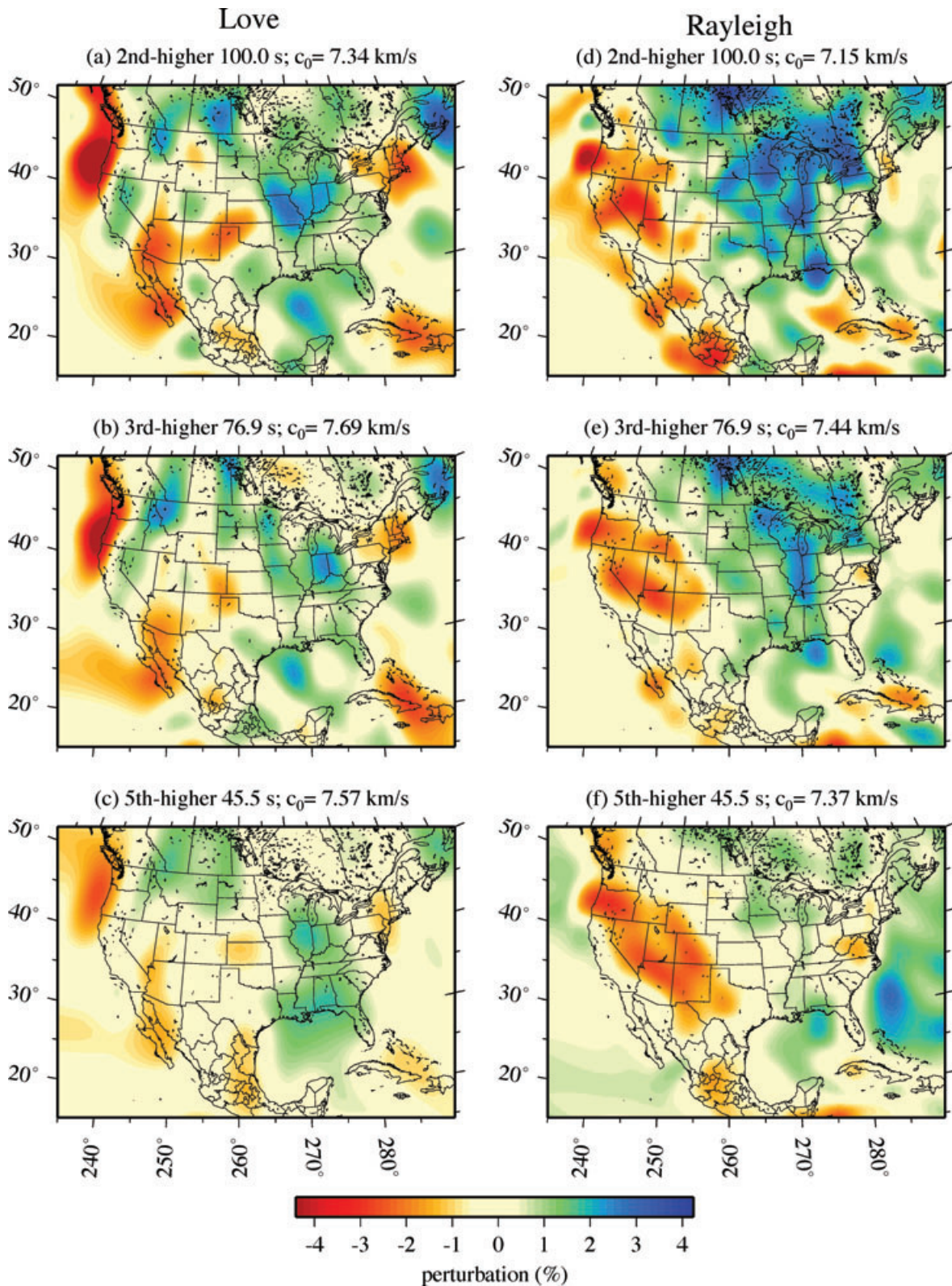


**Figure 17.** Higher mode phase speed maps of (a) second higher mode Love wave at 100 s, (b) third higher mode Love wave at 76.9 s, (c) fifth higher mode Love wave at 45.5 s, (d) second higher mode Rayleigh wave at 100 s, (e) third higher mode Rayleigh wave at 76.9 s and (f) fifth higher mode Rayleigh wave at 45.5 s.

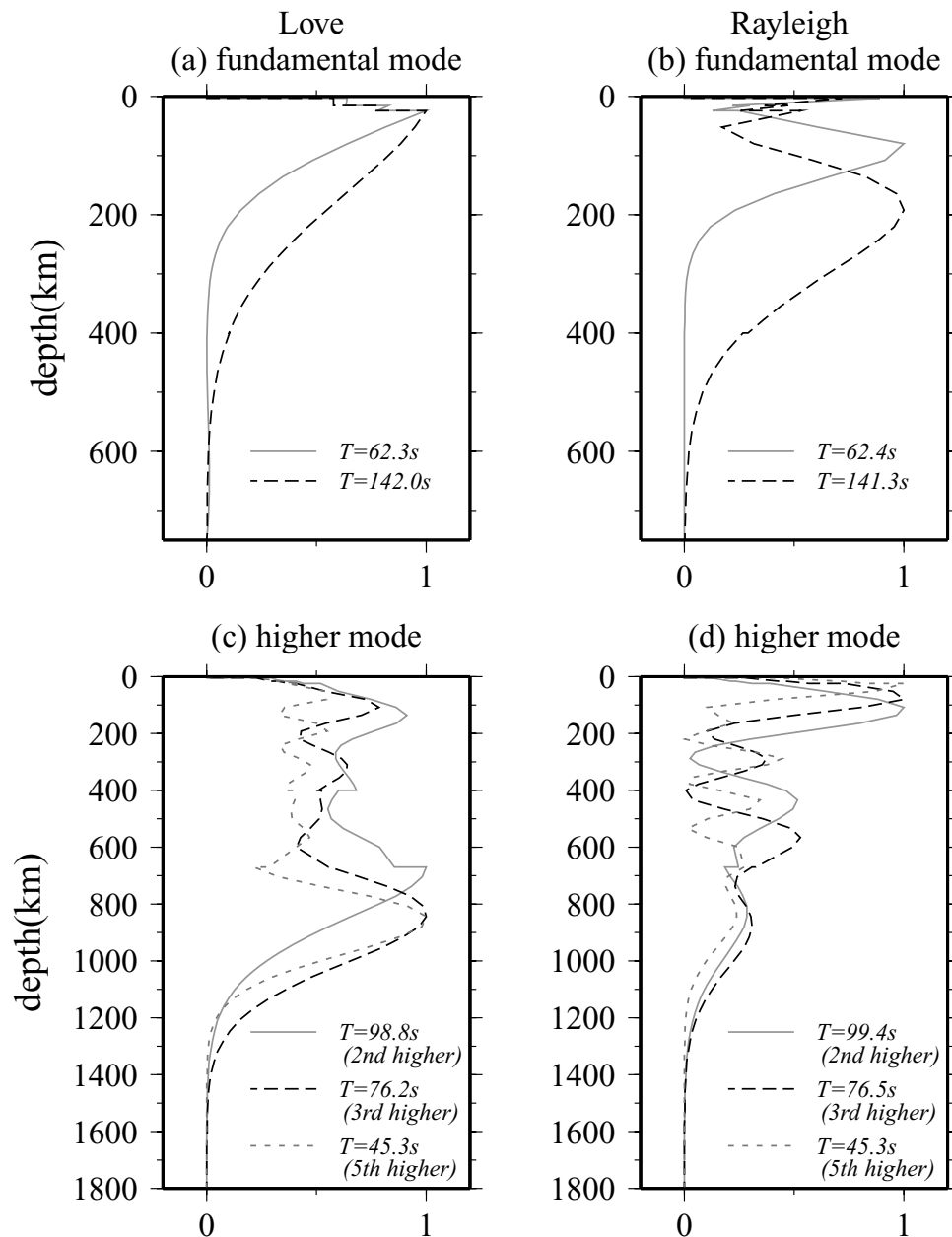


**Figure 18.** Sensitivity kernels for shear wave speed  $K_{\beta}$ , corresponding to the phase speed maps in Figs 16 and 17. (a) Fundamental mode Love waves at periods of 62.3 s and 142.0 s. (b) Fundamental mode Rayleigh waves at periods of 62.4 s and 141.3 s. (c) Second higher mode Love wave at 98.8 s, third higher mode Love wave at 76.2 s and fifth higher mode Love wave at 45.3 s. (d) Second higher mode Rayleigh wave at 99.4 s, third higher mode Rayleigh wave at 76.5 s and fifth higher mode Rayleigh wave at 45.3 s.

reasonable in terms of computation, and thus, it can be applied to very large data sets from high-density regional seismic arrays, such as the USArray of the EarthScope project.

It should be noted that the numbers of measurements for the higher modes tend to be smaller in the higher frequency range (Fig. 10). The reliability parameters, which practically constrain the numbers of available paths in this study, tend to be small for the shorter period range for the higher modes. This is likely a consequence of the limited number of seismic events below 100 km depth around North America, which typically generate large amplitudes of the higher modes. A contributing factor is also that, in the shorter period range, higher mode branches normally share a

similar group speed; that is, several mode branches arrive at the station nearly simultaneously at regional distances, and thus the modal contributions are difficult to separate. Although our method of fully non-linear fitting does not require the separation of mode branches in the time domain, we must keep in mind that the coupling between mode branches caused by lateral heterogeneity is apt to be more significant at shorter periods (e.g. Kennett 1995). Our data set of multimode phase speeds based on the automatic selection using the reliability parameter may reflect an appropriate range of frequency, for which several higher modes propagate independently. Thus, it seems possible that the higher modes in a certain frequency range, in which the strong effects of mode

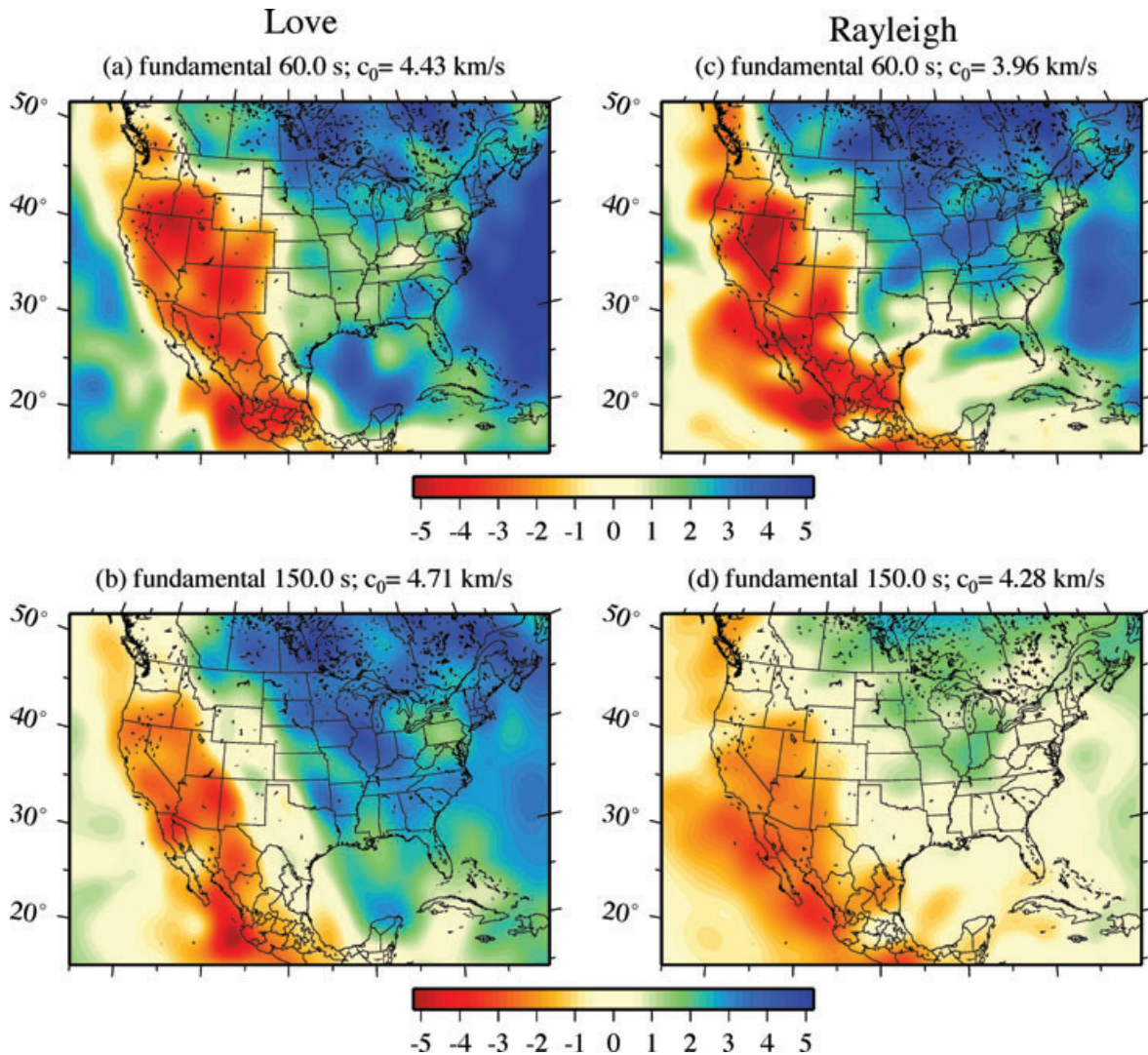


**Figure 19.** Fundamental-mode phase speed maps of Nettles (2005) in North America for (a) Love wave at 60.0 s, (b) Love wave at 150.0 s, (c) Rayleigh wave at 60.0 s and (d) Rayleigh wave at 150.0 s. These maps are represented as perturbations from a reference phase speed that is estimated from the average dispersion curves of a regional data set used in this study.

coupling are expected, are automatically eliminated from our set of measurements.

Despite such intrinsic limitations in the measurements of higher mode phase speeds, we were able to gather a large number of multimode phase speeds across a wide range of frequencies. The phase speed maps shown in this paper are preliminary, but we have achieved higher horizontal resolution of North American model compared to earlier studies of continental-scale models using long-period surface waves.

We have shown only phase speed maps of multimode Love and Rayleigh waves, since the main objective of this paper is to summarize the method of the automated multimode phase speed measurements and its application to data from the dense seismic network in the United States. The 3-D distribution of radially anisotropic shear wave speed structure can be obtained from the simultaneous inversions of the multimode Love and Rayleigh waves, which will be discussed in detail in future work.

The new automated method is useful for extracting the multimode surface wave phase speeds from a rapidly growing numbers of

seismic stations in the United States as well as many other places on the Earth, which will eventually be the basis for regional scale mapping of anisotropic heterogeneity in the upper mantle and the mantle transition zone.

#### ACKNOWLEDGMENTS

We thank Jeannot Trampert and Karin Visser for providing us with their global phase speed models, Meredith Nettles for providing her phase speed models of North America and Malcolm Sambridge for the provision of the NA code. Reviews by two anonymous reviewers were helpful to improve our original manuscript. KY is grateful to JSPS (Japan Society for the Promotion of Sciences) for a fellowship for conducting research in the United States. This study was partly supported by Grant-in-Aid for Scientific Research (No.17740283 and No.22654053) to K.Y. from the Ministry of Education, Culture, Sports, Science and Technology of Japan. All the figures were generated with the Generic Mapping Tools (Wessel & Smith 1998).

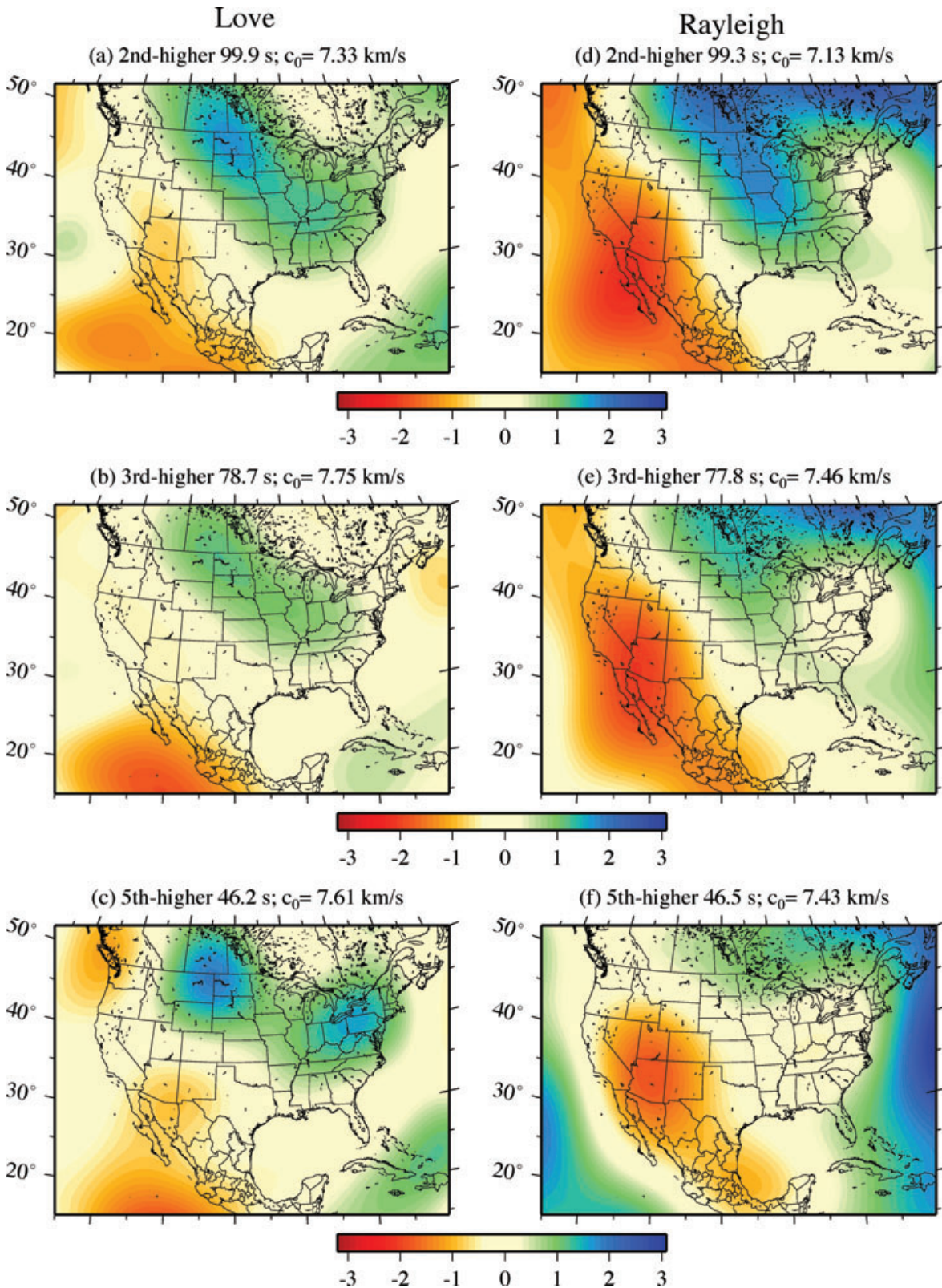


**Figure 20.** North American portion of global-scale isotropic phase speed maps of Visser *et al.* (2008) for (a) second higher mode Love wave at 99.9 s, (b) third higher mode Love wave at 78.7 s, (c) fifth higher mode Love wave at 46.2 s, (d) second higher mode Rayleigh wave at 99.3 s, (e) third higher mode Rayleigh wave at 77.8 s and (f) fifth higher mode Rayleigh wave at 46.5 s. These maps are represented as perturbations from a reference phase speed that is estimated from the average dispersion curves of a regional data set used in this study.

## REFERENCES

- Bedle, H. & van der Lee, S., 2009. *S* velocity variations beneath North America, *J. geophys. Res.*, **114**, B07308, doi:10.1029/2008JB005949.
- Bird, P., 2003. An updated digital model of plate boundaries, *Geochem. Geophys. Geosyst.*, **1027**, doi:10.1029/2001GC000252.
- Burdick, S. *et al.*, 2008. Upper mantle heterogeneity beneath North America from travel time tomography with global and USArray transportable array data, *Seism. Res. Lett.*, **79**, 384–392.
- Cara, M. & L ev eque, J.J., 1987. Waveform inversion using secondary observables, *Geophys. Res. Lett.*, **14**, 1046–1049.
- Dahlen, F.A. & Tromp, J., 1998. *Theoretical Global Seismology*, Princeton Univ. Press, Princeton, New Jersey.
- Debayle, E. & Kennett, B.L.N., 2000a. The Australian continental upper mantle: structure and deformation inferred from surface waves, *J. geophys. Res.*, **105**, 25 243–25 450.
- Debayle, E. & Kennett, B.L.N., 2000b. Anisotropy in the Australian upper mantle from Love and Rayleigh waveform inversion, *Earth planet. Sci. Lett.*, **184**, 339–351.
- Deschamps, F., Snieder, R. & Trampert, J., 2001. The relative density-to-shear velocity scaling in the uppermost mantle, *Phys. Earth planet. Inter.*, **124**, 193–211.
- Dziewonski, A.M. & Anderson, D.L., 1981. Preliminary reference Earth model, *Phys. Earth planet. Inter.*, **25**, 297–356.
- Dziewonski, A.M., Chou, T.-A. & Woodhouse, J.H., 1981. Determination of earthquake source parameters from waveform data for studies of global and regional seismicity, *J. geophys. Res.*, **86**, 2825–2852.
- Ekstr om, G., Tromp, J. & Larson, E.W.F., 1997. Measurements and global models of surface wave propagation, *J. geophys. Res.*, **102**, 8137–8157.
- Ekstr om, G., Dziewonski, A.M., Maternovskaya, N. & Nettles, M., 2005. Global seismicity of 2003: centroid-moment tensor solutions for 1087 earthquakes, *Phys. Earth planet. Inter.*, **148**, 327–351.
- Fichtner, A., Kennett, B.L.N., Igel, H. & Bunge, H.-P., 2008. Theoretical background for continental- and global-scale full-waveform inversion in the time-frequency domain, *Geophys. J. Int.*, **175**, 665–685.
- Fishwick, S., Heintz, M., Kennett, B.L.N., Reading, A.M. & Yoshizawa, K., 2008. Steps in lithospheric thickness within eastern Australia, evidence from surface wave tomography, *Tectonics*, **27**, TC4009, doi:10.1029/2007TC002116.
- Grubbs, F.E., 1969. Procedures for detecting outlying observations in samples, *Technometrics*, **11**, 1–21.
- Kennett, B.L.N., 1995. Approximations for surface-wave propagation in laterally varying media, *Geophys. J. Int.*, **122**, 470–478.
- Kennett, B.L.N. & Yoshizawa, K., 2002. A reappraisal of regional surface wave tomography, *Geophys. J. Int.*, **150**, 37–44.
- Kennett, B.L.N., Engdahl, E.R. & Buland, R., 1995. Constraints on seismic velocities in the Earth from traveltimes, *Geophys. J. Int.*, **122**, 108–124.
- Lebedev, S., Nolet, G., Meier, T. & van der Hilst, R.D., 2005. Automated multimode inversion of surface and S waveforms, *Geophys. J. Int.*, **162**, 951–964.
- Levshin, A.L., Barmin, M.P., Ritzwoller, M.H. & Trampert, J., 2005. Minor-arc and major-arc global surface wave diffraction tomography, *Phys. Earth planet. Inter.*, **149**, 205–223.
- Li, X. & Romanowicz, B., 1996. Global mantle shear velocity model developed using nonlinear asymptotic coupling theory, *J. geophys. Res.*, **101**, 22 245–22 273.
- Marone, F., Gung, Y. & Romanowicz, B., 2007. Three-dimensional radial anisotropic structure of the North American upper mantle from inversion of surface waveform data, *Geophys. J. Int.*, **171**, 206–222.
- Masters, G., Laske, G., Bolton, H. & Dziewonski, A.M., 2000. The relative behavior of shear velocity, bulk sound speed, and compressional velocity in the mantle: implications for chemical and thermal structure, in *Earth's Deep Interior: Mineral Physics and Tomography From the Atomic to the Global Scale*, Geophys. Monogr. Ser., Vol. 117, pp. 66–86, eds Karato, S. *et al.*, American Geophysical Union, Washington, DC.
- Montagner, J.-P. & Anderson, D.L., 1989. Petrological constraints on seismic anisotropy, *Phys. Earth planet. Inter.*, **54**, 82–105.
- Nataf, H.C. & Ricard, T., 1996. 3SMAC: an a priori tomographic model of the upper mantle based on geophysical modeling, *Phys. Earth planet. Inter.*, **95**, 101–122.
- Nettles, M., 2005. Anisotropic velocity structure of the mantle beneath North America, *PhD thesis*, Harvard University, Cambridge MA, USA, 253 pp.
- Nettles, M. & Dziewonski, A.M., 2008. Radially anisotropic shear velocity structure of the upper mantle globally and beneath North America, *J. geophys. Res.*, **113**, B02303, doi:10.1029/2006JB004819.
- Nolet, G., 1990. Partitioned waveform inversion and two-dimensional structure under the network of autonomously recording seismographs, *J. geophys. Res.*, **95**, 8499–8512.
- Paige, C.C. & Saunders, M.A., 1982. LSQR: an algorithm for sparse linear equations and sparse least squares, *ACM Trans. Math. Software*, **8**, 43–71.
- Resovsky, J. & Trampert, J., 2003. Using probabilistic seismic tomography to test mantle velocity-density relationships, *Earth planet. Sci. Lett.*, **215**, 121–134.
- Ritzwoller, M.H., Shapiro, N.M., Barmin, M.P. & Levshin, A.L., 2002. Global surface wave diffraction tomography, *J. geophys. Res.*, **107**, 2335, doi:10.1029/2002JB001777.
- Sambridge, M., 1999a. Geophysical inversion with a Neighbourhood Algorithm -I. Searching a parameter space, *Geophys. J. Int.*, **138**, 479–494.
- Sambridge, M., 1999b. Geophysical inversion with a Neighbourhood Algorithm -II. Appraising the ensemble, *Geophys. J. Int.*, **138**, 727–746.
- Sigloch, K., McQuarrie, N. & Nolet, G., 2008. Two-stage subduction history under North America inferred from multiple-frequency tomography, *Nature Geoscience*, **1**, 458–462.
- Stutzmann, E. & Montagner, J.-P., 1993. An inverse technique for retrieving higher mode phase velocity and mantle structure, *Geophys. J. Int.*, **113**, 669–683.
- Takeuchi, N., 2007. Whole mantle SH velocity model constrained by waveform inversion based on three-dimensional Born kernels, *Geophys. J. Int.*, **169**, 1153–1163.
- Trampert, J. & Woodhouse, J.H., 1995. Global phase velocity maps of Love and Rayleigh waves between 40 and 150 seconds, *Geophys. J. Int.*, **122**, 675–690.
- Tromp, J. & Dahlen, F.A., 1992. Variational principles for surface wave propagation on a laterally heterogeneous Earth - II. Frequency-domain JWKB theory, *Geophys. J. Int.*, **109**, 599–619.
- van der Lee, S. & Frederiksen, A., 2005. Surface wave tomography applied to the North American upper mantle, in *Seismic Earth - Array analysis of broadband seismograms*, Geophys. Monogr. Ser., Vol. 157, pp. 67–80, eds Levander, A. & Nolet, G., American Geophysical Union, Washington, DC.
- van der Lee, S. & Nolet, G., 1997. Seismic image of the subducted trailing fragments of the Farallon plate, *Nature*, **386**, 266–269.
- van Heijst, H.J. & Woodhouse, J.H., 1997. Measuring surface-wave overtone phase velocities using a mode-branch stripping technique, *Geophys. J. Int.*, **131**, 209–230.
- van Heijst, H.J. & Woodhouse, J., 1999. Global high-resolution phase velocity distributions of overtone and fundamental-mode surface waves determined by mode branch stripping, *Geophys. J. Int.*, **137**, 601–620.
- Visser, K., 2008. Monte Carlo search techniques applied to the measurements of higher mode phase velocities and anisotropic surface wave tomography, *PhD thesis*, Utrecht University, the Netherlands.
- Visser, K., Lebedev, S., Trampert, J. & Kennett, B.L.N., 2007. Global Love wave overtone measurements, *Geophys. Res. Lett.*, **34**, L03302, doi:10.1029/2006GL028671.
- Visser, K., Trampert, J. & Kennett, B.L.N., 2008. Global anisotropic phase velocity maps for higher mode Love and Rayleigh waves, *Geophys. J. Int.*, **172**, 1016–1032.
- Wang, Z. & Dahlen, F.A., 1995. Spherical-spline parameterization of three-dimensional Earth models, *Geophys. Res. Lett.*, **22**, 3099–3102.
- Wessel, P. & Smith, W.H.F., 1998. New, improved version of the Generic Mapping Tools released, *EOS, Trans. Am. geophys. Un.*, **79**, 579.
- Woodhouse, J.H., 1974. Surface waves in a laterally varying layered structure, *Geophys. J. R. astr. Soc.*, **37**, 461–490.

Yoshizawa, K. & Kennett, B.L.N., 2002a. Non-linear waveform inversion for surface waves with a neighbourhood algorithm: application to multimode dispersion measurements, *Geophys. J. Int.*, **149**, 118–133.  
Yoshizawa, K. & Kennett, B.L.N., 2002b. Determination of the influence zone for surface wave paths, *Geophys. J. Int.*, **149**, 440–453.  
Yoshizawa, K. & Kennett, B.L.N., 2004. Multi-mode surface wave tomography for the Australian region using a three-stage approach in-

corporating finite frequency effects, *J. geophys. Res.*, **109**, B02310, doi:10.1029/2002JB002254.  
Yoshizawa, K. & Kennett, B.L.N., 2005. Sensitivity kernels for finite-frequency surface waves, *Geophys. J. Int.*, **162**, 910–926.  
Zhou, Y., Dahlen, F.A. & Nolet, G., 2004. Three-dimensional sensitivity kernels for surface wave observables, *Geophys. J. Int.*, **158**, 142–168.